

Effects of Oxidation of Top and Bottom Interface on the Electric, Magnetic, and Spin-Orbit Torque Properties of Pt/Co/AlO_x Trilayers

Junxiao Feng, Eva Grimaldi, Can Onur Avci,

Manuel Baumgartner, Giovanni Cossu, Antonella Rossi, and Pietro Gambardella

Department of Materials, ETH Zurich, 8093 Zurich, Switzerland

(Dated: February 23, 2022)

Oxidation strongly influences the properties of magnetic layers employed in spintronic devices. We studied the effect of oxidation on the structural, magnetic, and electrical properties as well as current-induced spin-orbit torques (SOT) in Pt/Co/AlO_x, Pt/CoO_x/Co/AlO_x, and PtO_x/Co/AlO_x layers. We show how the saturation magnetization, perpendicular magnetic anisotropy, anomalous Hall resistance, and SOT are systematically affected by the degree of oxidation of both the Pt/Co and Co/Al interfaces. Oxidation of the Co/Al interface results in a 21% and 42% variation of the damping-like and field-like SOT efficiencies, which peak at 0.14 and 0.07, respectively. The insertion of a paramagnetic CoO_x layer between Pt and Co maintains a very strong perpendicular magnetic anisotropy and improves the damping-like and field-like SOT efficiencies, up to 0.26 and 0.20, respectively. In contrast with recent reports, we do not find that the oxidation of Pt leads to a significant enhancement of the torques. Rather, we find that oxygen migrates from Pt to the Co and Al layers, leading to a time-dependent oxidation profile and an effective spin Hall conductivity that decreases with increasing oxygen concentration. Finally, we studied current-induced switching in Pt/Co/AlO_x with different degrees of oxidation and found a linear relationship between the critical switching current and the effective magnetic anisotropy controlled by the oxidation of Al. These results highlight the importance of interfaces and oxidation effects on the SOT and magnetotransport properties of heavy metal/ferromagnet/oxide trilayers, and provide information on how to improve the SOT efficiency and magnetization-switching characteristics of these systems.

I. INTRODUCTION

Heavy metal/ferromagnet/oxide (HM/FM/Ox) trilayers are a fundamental component of spintronic devices [1–4] due to their tunable perpendicular magnetic anisotropy (PMA) [5], relatively high Curie temperature [6], fast dynamics [7], and compatibility with back-end-of-line CMOS processes [8, 9]. In recent years, current-induced spin-orbit torques (SOT) have emerged as a powerful tool to manipulate the magnetization of these systems [10–17]. SOT rely on the spin Hall effect of the HM as well as on Rashba-type interfacial effects in order to convert an in-plane charge current into a non-equilibrium spin accumulation, which diffuses into the FM and transfers angular momentum to the local magnetization via the *s-d* exchange interaction [17]. Symmetry considerations show that the current-induced spin accumulation allows for two types of torques, namely the damping-like and field-like SOT [14, 18].

Several studies have shown that modifying the interface oxidation in HM/FM/Ox trilayers leads to substantial changes of the magnetic properties. Early reports focused on the effect of interface oxidation on the magnetic anisotropy [5, 19–22]. Following the discovery of SOT, the focus has shifted towards using oxidation as a tool to modify the SOT and current-induced switching characteristics by either engineering the oxidation of the top layer during growth [11, 23–29] or post-growth dynamic modification of the oxidation profile by applying a gate voltage [30–32].

Very recently, the oxidation of the HM layer has been found to dramatically improve the SOT effi-

ciency of trilayer structures such as W/CoFeB/TaN [33], Pt/Ni₈₁Fe₁₉/SiO₂ [34], and Pt/CoTb/MgO [35]. In PtO_x/Ni₈₁Fe₁₉/SiO₂, the SOT efficiency reaches a maximum of 0.9 for fully oxidized Pt, which implies that most of the charge current is converted into a spin current, even though no current actually flows through Pt [34]. All of these studies focused on the oxidation of one interface only, leaving open questions in regard to the effects of oxidation on either interface of the same system or on the FM itself. Further, the strong increase of the SOT efficiency reported for oxidized Pt is very promising as a means to achieve switching at low current density, but needs to be confirmed in other systems, particularly in trilayers exhibiting PMA.

In this article, we report a systematic study of the effects of oxidation on the structural, electrical, and magnetic properties of Pt/Co/AlO_x trilayers, as well as of the current-induced SOT and magnetization switching characteristics. We find that oxidation of the Co/Al and Pt/Co interfaces, and of the Co layer itself, influences the above properties in distinct ways. More specifically, we find that oxidation of either the Co/Al or Pt/Co interface has a sizeable effect on the SOT. The strongest effects is observed upon oxidation of the Pt/Co interface, pinpointing the critical role of this interface in the spin currents giving rise to the SOT. The insertion of a thin CoO_x layer next to Pt leads to a 100% increase of the SOT efficiency for both damping-like and field-like torques, whereas structures with oxidized Pt present significantly lower efficiencies compared to Pt/Co/AlO_x and recent studies [34, 35]. Additionally, we find that, while a single layer of PtO_x remains stable after oxidation, PtO_x

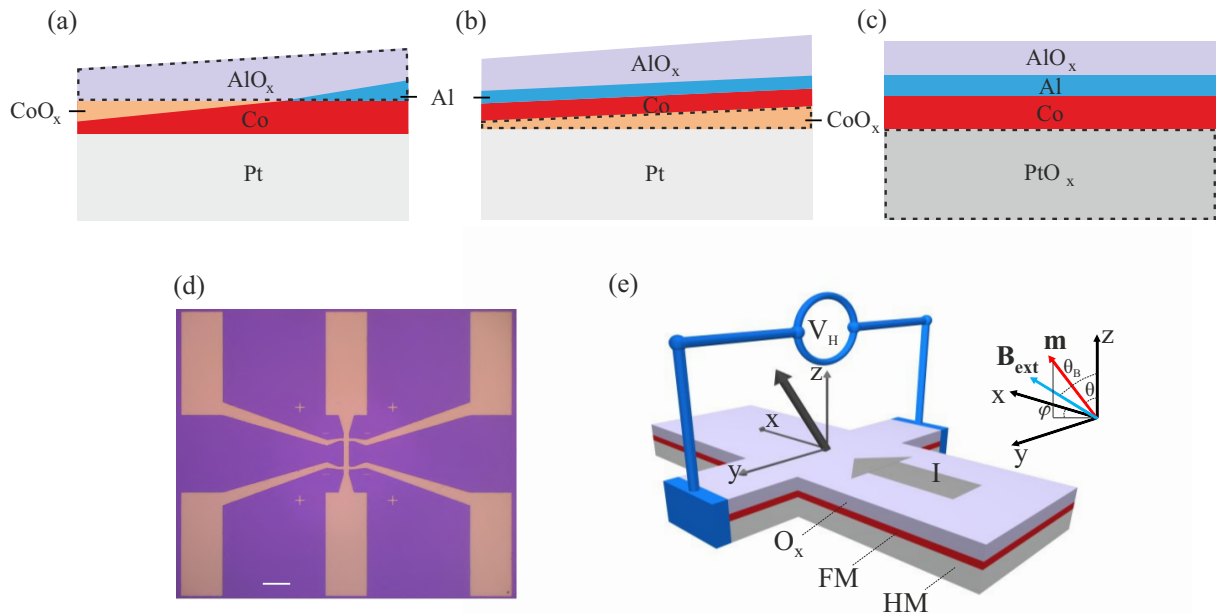


FIG. 1. Schematic cross-section of the samples employed in this study: (a) Pt/Co/AlO_x, (b) Pt/CoO_x/Co/AlO_x and (c) PtO_x/Co/AlO_x. (d) Micrograph of a patterned Hall bar after photolithography. The scale bar is 50 μm . (e) Schematic diagram of the experimental geometry and coordinate system. A positive current is injected along the x direction, \mathbf{m} is the unitary magnetization and \mathbf{B}_{ext} is the external field.

is strongly reduced upon deposition of the Co/Al overlays due to oxygen diffusion towards Co and Al. Finally, we show that the oxidation of Al can be used to tune the critical current for switching of the Co layer, which is directly proportional to the strength of the perpendicular magnetic anisotropy controlled by oxidation. These results highlight the importance of tuning and preserving the oxidation profiles in HM/FM/Ox trilayers in order to control the SOT efficiency and magnetic anisotropy of these systems.

II. SAMPLE CHARACTERIZATION

A. Sample fabrication

We grew three series of samples on Si₃N₄ wafers using dc magnetron sputtering with base pressure $< 8.0 \times 10^{-8}$ Torr and Ar pressure between 0.3 and 1.1 mTorr. The first series, which we refer to as Pt/Co/AlO_x, was obtained by depositing an Al wedge with thickness 12.8 - 19.5 \AA on a Pt(5)/Co(1) bilayer (the numbers between parentheses represent the thickness in nm). After deposition of the full metallic stack, an oxygen plasma with 10.0 mTorr pressure and 53 W power was used to oxidize the Al wedge with the purpose of obtaining over- and under-oxidized regions of the top Co interface [Fig. 1(a)]. We note that the easy magne-

tization axis is perpendicular to the sample plane for an Al thickness $t_{\text{Al}} = 13.4 - 18.9 \text{ \AA}$, whereas beyond this range the easy axis is in-plane, in agreement with previous reports [5, 19, 20]. The second series is Pt(5)/CoO_x(t_{CoO_x})/Co(0.65)/AlO_x(1.85), which was grown by depositing a CoO_x wedge layer with thickness $t_{\text{CoO}_x} = 2.1 - 4.9 \text{ \AA}$ on Pt by reactive sputtering of Co with an O₂:(Ar+O₂) ratio of 50% [Fig. 1(b)]. In this series, t_{Al} was fixed at 1.85 nm in order to ensure PMA for all the samples. The third series is PtO_x(5)/Co(1)/AlO_x(2.5) [Fig. 1(c)]. Unlike the first two series, which have a wedge structure, this series includes seven different samples grown with an O₂:(Ar+O₂) ratio ranging between 0 and 60% during deposition of the Pt layer. All the samples of the third series have in-plane magnetic anisotropy (IMA) resulting from the under-oxidation of the relatively thick Al cap layer. This choice was made in order to have the same type of magnetic anisotropy in the series, since we found that the oxidation of Pt reduces the PMA of the PtO_x/Co interface relative to Pt/Co. As reference for the XPS and electrical measurements, we also deposited single PtO_x(5) layers on Si₃N₄ with the same O₂:(Ar + O₂) ratios as used for the full PtO_x/Co/AlO_x trilayers. These reference samples are not capped in order to avoid oxygen migration effects. Contact with air is unlikely to influence the oxygen distribution in single PtO_x layers deposited by reactive sputtering, consistently with the observation

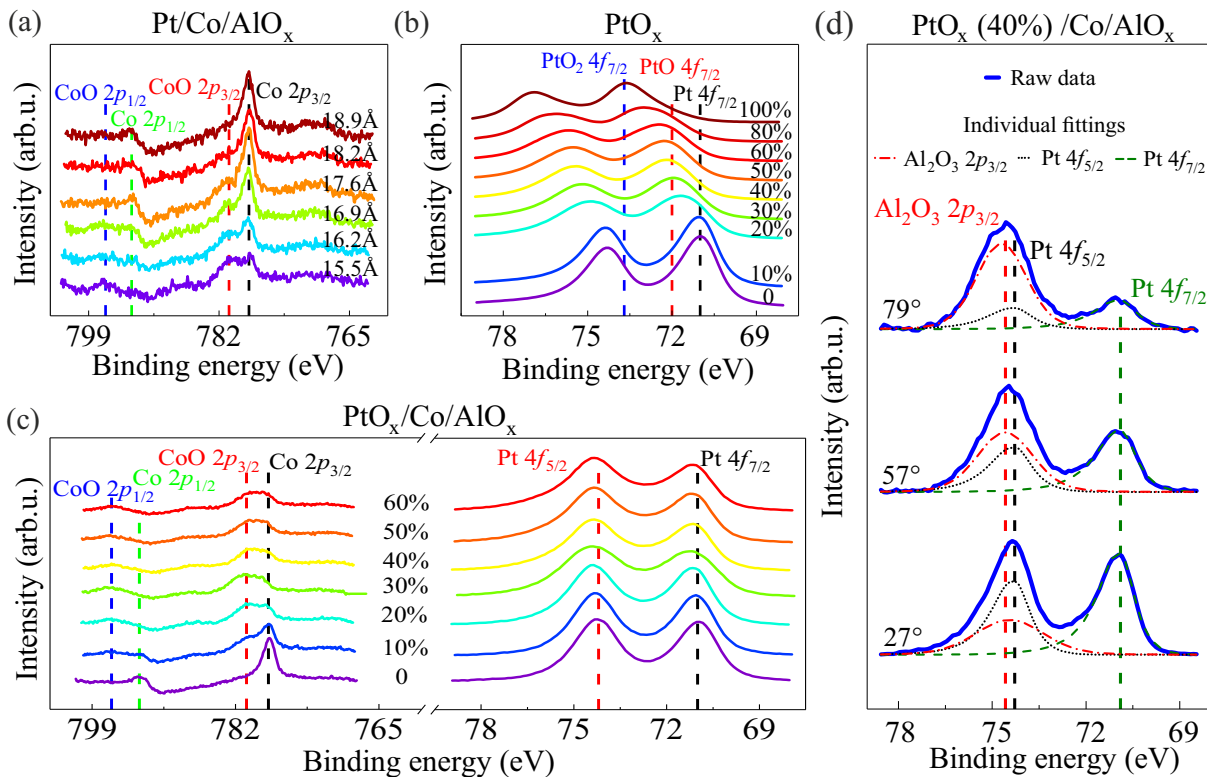


FIG. 2. XPS spectra of (a) Co in Pt/Co/AlO_x(*t*_{Al}), (b) Pt in PtO_x single layers with different O₂:(Ar+O₂) ratio, and (c) Co and Pt in PtO_x/Co/AlO_x with different O₂:(Ar+O₂) ratio. (d) Angle-resolved XPS of the Al 2*p* and Pt 4*f* peaks in PtO_x(40%)/Co/AlO_x recorded for three incident angles with respect to the sample’s surface normal. The dashed and dotted lines show the intensity of the individual peaks derived from a fit of the experimental spectrum (solid line). The dotted (green) and dashed (red) lines show the model Gaussian/Lorentzian functions used to resolve the contributions of the overlapping photoelectron signals.

that the resistance remains constant after deposition.

The Pt layers are polycrystalline with [111] preferred orientation, as confirmed by transmission Kikuchi diffraction. After deposition, all the samples were diced in two pieces, one for the characterization of the structure and magnetization properties and the other for device patterning and SOT measurements. The devices are 10 μm wide and 50 μm long Hall bars defined by optical lithography followed by Ar milling [Fig. 1(d)]. The coordinate system employed throughout this study is depicted in Fig. 1(e).

B. XPS

We performed x-ray photoemission spectroscopy (XPS) in order to characterize the oxidation state of the first and third series described above. Figure 2(a) shows the XPS spectra of Pt/Co/AlO_x recorded by measuring photoemission from the Co 2*p*_{1/2} and 2*p*_{3/2} core levels of samples with different *t*_{Al}. The spectra of samples with *t*_{Al} > 17.6 Å present two peaks at 778.1 and 793.4 eV, which are characteristic of metallic Co. On the other hand, the spectra of samples with *t*_{Al} < 17.6 Å show

high energy shoulders at 780.7 and 796.7 eV characteristic of CoO [19], the intensity of which increases with decreasing Al thickness. These measurements show that the Co/Al interface is underoxidized and that Co remains fully metallic down to *t*_{Al} = 17.6 Å, after which CoO forms. We designate the sample with *t*_{Al} = 17.6 Å as the “optimized” sample for which the Co/Al interface is fully oxidized, but Co is not, leading to maximum PMA.

In order to characterize the third series, we first measured as a reference the XPS spectra of single PtO_x(5) layers. The spectra, reported in Fig. 2(b), show the evolution of the Pt 4*f*_{7/2,5/2} doublet with increasing O₂ partial pressure. As the peak of the Pt 4*f*_{5/2} level overlaps with the Al 2*p* level around 74.6 eV, typical of Al₂O₃ [36], we focus on the behavior of the 4*f*_{7/2} peak. This peak shifts from 71 eV below 10% O₂, as typical of Pt, to 72 eV around 40% O₂, characteristic of PtO, and finally to 73.7 eV at 100% O₂, indicating the formation of PtO₂ [34]. These spectra confirm that a single layer of Pt can be stably oxidized by controlling the amount of O₂ during sputtering. However, the measurements of the full PtO_x/Co/AlO_x stack that were performed 6 days after deposition, shown in Fig. 2(c), reveal quite a different picture. In these samples, the Pt 4*f*_{7/2} peak does not

shift with increasing O_2 partial pressure, showing that Pt is not oxidized. On the other hand, a strong shift of the Co $2p$ peaks is observed, indicating the formation of CoO upon diffusion of oxygen into Co from the Pt side.

The progressive oxidation of the top layers resulting from oxygen diffusion was further confirmed by angle-resolved XPS, as shown in Fig. 2(d) for $PtO_x(40\%)/Co/AlO_x$. The spectra recorded with an increasing emission angle relative to the surface normal, from 27° to 79° , have a higher degree of surface sensitivity. These spectra reveal a progressive increase of the Al_2O_3 intensity relative to Pt, showing that Al is strongly oxidized, whereas the position of the Pt peak does not change as a function of incidence angle. Note that $t_{Al} = 25 \text{ \AA}$ in this series, such that Al was supposed to be underoxidized. Overall, these observations indicate that PtO_x layers are not stable when embedded in a multilayer structure, as oxygen tends to diffuse away from Pt and oxidize both the Co and Al layers. Such a behavior can be rationalized in terms of the enthalpy of formation of PtO_x (-101.3 kJ/mol) [37], which is significantly lower than that of AlO_x (-1675.7 kJ/mol) [38] and CoO_x (-237.4 kJ/mol) [39].

C. Electrical resistance

Figure 3 summarizes the electrical resistance of devices belonging to the three series and of PtO_x single layers. The typical device resistance of $Pt/Co/AlO_x$ is $0.33\text{-}0.34 \text{ k}\Omega$, which corresponds to a resistivity of $40\text{-}41 \mu\Omega\text{cm}$ by assuming that only Pt and Co are conductive. This assumption is corroborated by the weak dependence of the resistance on t_{Al} [Fig. 3(a)], which shows that the oxidation state of the top Co/Al interface does not influence significantly the conductivity of $Pt/Co/AlO_x$.

Devices belonging to the $Pt/CoO_x/Co/AlO_x$ series have a resistance of $0.35\text{-}0.36 \text{ k}\Omega$, which corresponds to a resistivity of $40\text{-}41 \mu\Omega\text{cm}$. Also in this case we assume that only Pt and Co are conductive. Note that the resistance is approximately constant as a function of t_{CoO_x} , suggesting that CoO_x is weakly conducting or effectively an insulator [Fig. 3(b)]. From these two sets of data we conclude that the oxidation of the Co/Al and Pt/Co interfaces does not have a major impact on the resistivity, indicating that conduction is dominated by the 5 nm-thick Pt channel.

The resistances of the reference PtO_x layers are shown in Fig. 3(c) as a function of $O_2:(Ar+O_2)$ ratio. The resistance of PtO_x increases dramatically with increasing O_2 ratio (note the log scale of the plot), indicating that PtO_x becomes nearly insulating for $50\text{-}60\%$ of O_2 . These results are consistent with the conclusions drawn from the XPS spectra presented in Fig. 2(b). In contrast with the reference PtO_x layers, the resistance of $PtO_x/Co/AlO_x$ saturates around 40% of O_2 rather than increasing monotonically with O_2 ratio, to a value that is about two orders of magnitude lower compared to PtO_x

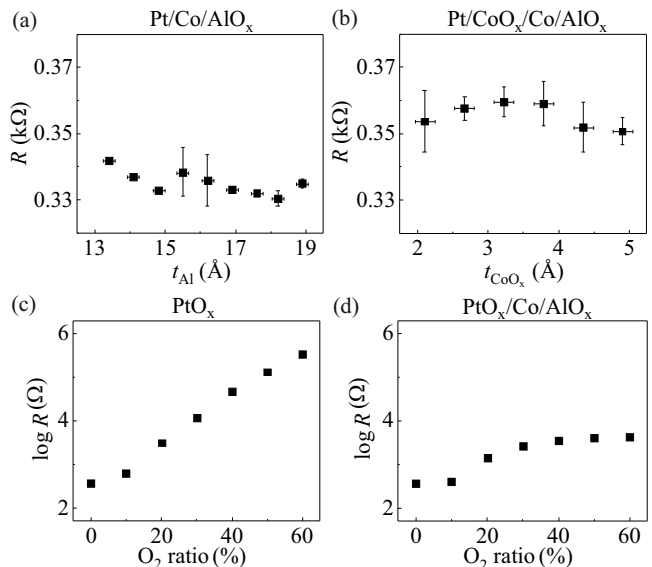


FIG. 3. 4-point resistance as a function of (a) t_{Al} in $Pt/Co/AlO_x$, (b) t_{CoO_x} in $Pt/CoO_x/Co/AlO_x$, and $O_2:(Ar+O_2)$ ratio in (c) PtO_x single layers and (d) $PtO_x/Co/AlO_x$. Vertical error bars represent the standard deviation of the average of different devices from the same series. Horizontal error bars represent the uncertainty of the thickness calibration.

single layers. These findings corroborate the oxygen diffusion scenario outlined in Sec. II B.

III. MAGNETIC PROPERTIES

A. Saturation magnetization

We measured the total magnetic moment of each sample using superconducting quantum interference device (SQUID) magnetometry in an out-of-plane external field [see inset of Fig. 4(a) for an example of a magnetization curve]. The saturation magnetization M_s is obtained by dividing the saturation magnetic moment by the nominal volume of the Co layer. Figures 4(a-c) show how M_s varies in the three series.

In $Pt/Co/AlO_x$, M_s increases with increasing t_{Al} until it saturates around $t_{Al} = 17.6 \text{ \AA}$ [Fig. 4(a)]. This behavior is consistent with the formation of CoO with antiferromagnetic correlations for $t_{Al} < 17.6 \text{ \AA}$ and the metallic character of Co evidenced by XPS for $t_{Al} \geq 17.6 \text{ \AA}$.

In $Pt/CoO_x/Co/AlO_x$, M_s decreases monotonically as a function of t_{CoO_x} [Fig. 4(b)], which we ascribe to several factors. First, some of the oxygen initially present in CoO_x likely diffused into the metallic Co part, thus reducing M_s . Since the total amount of oxygen is proportional to t_{CoO_x} and t_{Co} is fixed, we expect that this effect becomes more pronounced with increasing t_{CoO_x} . Second, the deposition of a CoO_x layer between Pt and Co strongly reduces the proximity magnetization in Pt,

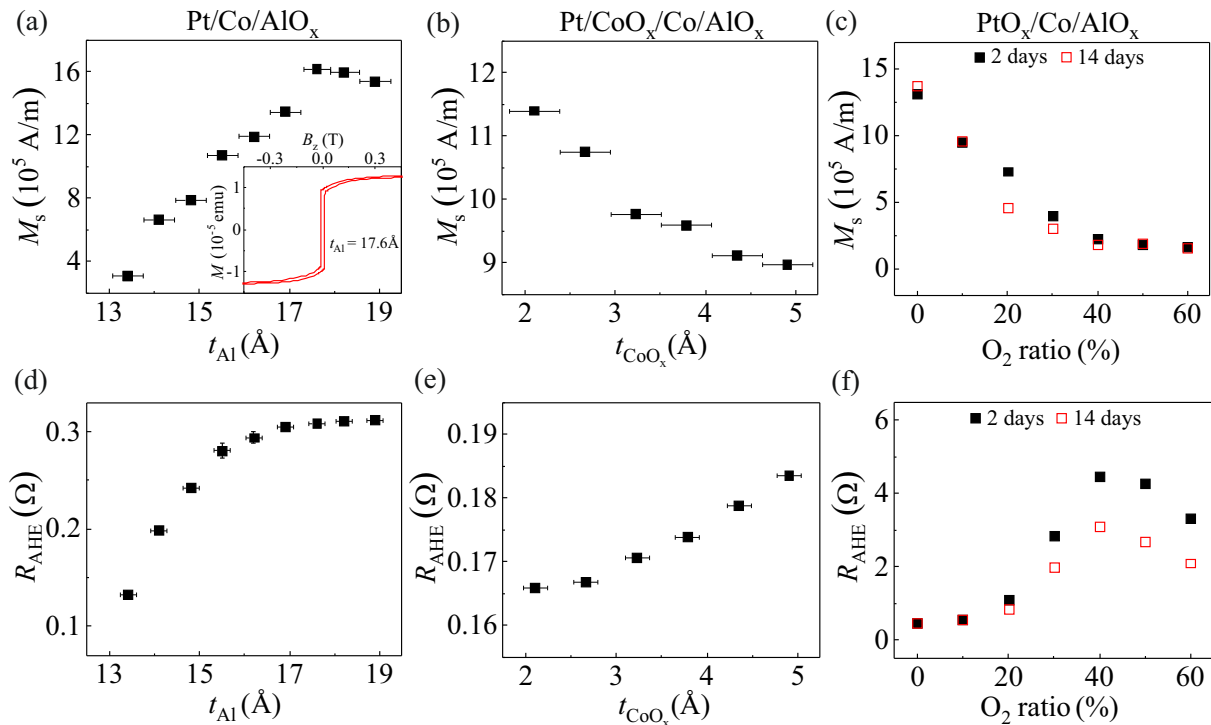


FIG. 4. Saturation magnetization as a function of (a) t_{Al} in Pt/Co/AlO_x, (b) t_{CoO_x} in Pt/CoO_x/Co/AlO_x, and (c) O₂:(Ar+O₂) ratio in PtO_x/Co/AlO_x. The inset in (a) shows the total magnetic moment of Pt/Co/AlO_x with $t_{\text{Al}} = 17.6 \text{ \AA}$ as a function of out-of-plane external field. (d-f) Same as (a-c) for the anomalous Hall resistance. The data shown as solid and open symbols in (c) and (f) were obtained, respectively, 2 and 14 days after the deposition of PtO_x/Co/AlO_x. Vertical error bars represent the standard deviation of the average of different devices from the same series. Horizontal error bars represent the uncertainty of the thickness calibration.

thus reducing M_s . Based on measurements of M_s in Pt/Co bilayers separated by ultrathin metal spacers, we estimate the latter effect to account for a loss of about $2 \times 10^5 \text{ A/m}$ [40].

In PtO_x/Co/AlO_x, M_s decreases by about a factor 7 as the O₂ ratio increases from 0 to 40% and beyond [Fig. 4(c)]. This trend is consistent with the significant diffusion of oxygen into the metallic Co layer evidenced by XPS as well as with the resistance measurements presented above. Measurements of PtO_x/Co/AlO_x performed 2 and 14 days after growth [solid and open symbols in Fig. 4(c)] further show that M_s changes with time for the intermediate oxidation ratios (20-40%), suggesting that oxygen diffusion is a relatively slow process.

B. Anomalous Hall resistance

The anomalous Hall effect (AHE) was measured by using the harmonic Hall voltage method described in Refs. 14 and 41. Representative AHE measurements for the different samples are reported in the Appendix. Figures 4(d-f) show the anomalous Hall resistance coefficient R_{AHE} in the three sample series. In the Pt/Co/AlO_x series, we find that R_{AHE} increases and then saturates as a function of t_{Al} , similar to M_s [Fig. 4(d)]. This

behavior shows that R_{AHE} depends on the volume fraction of metallic Co, which increases with increasing t_{Al} . Additionally, we observe that R_{AHE} approaches saturation faster than M_s , indicating that the AHE increases upon interfacial oxidation of Co, in agreement with previous work [43], which we attribute to enhanced electron scattering at the Co/AlO_x interface. In the Pt/CoO_x/Co/AlO_x series, we find that R_{AHE} increases monotonically with t_{CoO_x} , opposite to the behavior of M_s [Fig. 4(e)]. Although the relative change of R_{AHE} is small, this observation corroborates the conclusion that moderate oxidation of the Co interfaces, and possibly of the Co grain boundaries, enhances the AHE. These results are consistent with a previous study of the AHE in MgO/[Co/Pt]₃/MgO multilayers, which evidenced an increase of R_{AHE} upon insertion of a CoO_x layer between MgO and Co [44].

The strongest increase of R_{AHE} , by more than one order of magnitude, is found in PtO_x/Co/AlO_x. In this series, R_{AHE} reaches a maximum of 4.5 Ω around 40% O₂ ratio, compared to 0.3 Ω in Pt/Co/AlO_x, and decreases afterwards [Fig. 4(f)]. This nonmonotonic behavior suggests that, in the lower oxidation range (0-40%), the higher resistivity of Pt causes a larger current flow through Co, thereby increasing R_{AHE} . The turning point at 40% and successive decrease of R_{AHE} can then be at-

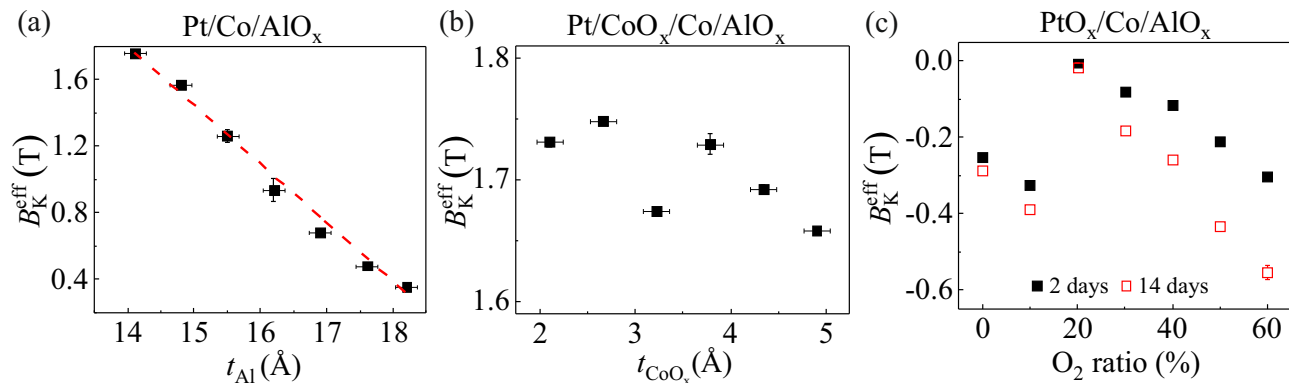


FIG. 5. Effective magnetic anisotropy field as a function of (a) t_{Al} in Pt/Co/AlO_x, (b) t_{CoO_x} in Pt/CoO_x/Co/AlO_x, and (c) O₂:(Ar+O₂) ratio in PtO_x/Co/AlO_x. The dashed line in (a) is a linear fit to the data. The solid and open symbols in (c) refer to measurements carried out 2 and 14 days after the deposition, respectively. Vertical error bars represent the standard deviation of the average of different devices from the same series. Horizontal error bars represent the uncertainty of the thickness calibration.

tributed to the strong reduction of M_s that occurs with the progressive oxidation of Co [Fig. 4(c)]. In this case, the difference between samples measured 2 and 14 days after deposition is substantial, which shows that changes in the oxidation profile influence the Hall conductivity more strongly than M_s .

C. Magnetic anisotropy

The magnetic anisotropy was characterized by measuring the effective anisotropy field B_K^{eff} . For samples with either uniaxial or easy plane anisotropy, this field is given by

$$B_K^{\text{eff}} = B_K + B_{\text{dem}} = \frac{2}{\mu_0 M_s} K - \mu_0 M_s, \quad (1)$$

where K is the anisotropy constant, including the effects of the magnetocrystalline and interface anisotropy, μ_0 the permeability of vacuum, and the last term represents the demagnetizing field of a thin film. Following Eq. 1, samples with PMA have $B_K^{\text{eff}} > 0$, whereas samples with IMA have $B_K^{\text{eff}} < 0$.

Both Pt/Co/AlO_x and Pt/CoO_x/Co/AlO_x present PMA with a dominant uniaxial behavior. B_K^{eff} was measured by fitting the anomalous Hall resistance as a function of a magnetic field applied perpendicular to the easy axis, as detailed in the Appendix. Figure 5(a) shows B_K^{eff} as a function of t_{Al} in the Pt/Co/AlO_x series. With increasing t_{Al} , B_K^{eff} decreases almost in a linear fashion from 1.7 T to 0.4 T; samples with $t_{\text{Al}} > 18.9$ Å have in-plane magnetization. This trend is attributed to the linear increase of M_s in the over-oxidized range ($t_{\text{Al}} = 13.4$ - 16.9 Å) [Fig. 4(a)]. In this range, the top and bottom interfaces do not change significantly so that B_K^{eff} is mostly affected by the change of the demagnetizing field, which is directly proportional to M_s . In the optimally-oxidized and under-oxidized range ($t_{\text{Al}} = 17.6$ - 18.9 Å),

M_s remains approximately constant, but the oxidation of the top Co interface (higher Co/Al interface anisotropy $K_i^{\text{Co/Al}}$) leads to an increase of the PMA [45].

In the Pt/CoO_x/Co/AlO_x series, B_K^{eff} remains close to 1.7 T in the entire CoO_x thickness range [Fig. 5(b)], despite the moderate decrease of M_s as a function of t_{CoO_x} [Fig. 4(b)]. We attribute this behavior to the strong PMA induced by the CoO_x/Co interface, as suggested by previous studies [46, 47].

The samples belonging to the PtO_x/Co/AlO_x series have IMA. B_K^{eff} in this case was estimated by the magnetic field required to saturate the sample in the hard out-of-plane direction, as described in Ref. 40. Figure 5(c) shows B_K^{eff} as a function of the O₂ ratio measured 2 and 14 days after deposition. We identify two different regimes below and above 20% of O₂. B_K^{eff} decreases going from 0 to 10% O₂, presumably due to the oxidation of Pt at the Pt/Co interface at this low O₂ concentration. However, at 20% O₂ ratio B_K^{eff} suddenly approaches zero and then decreases again for larger O₂ ratios. One plausible explanation of this peculiar behavior is that oxygen diffuses through Co up to the Al interface with increasing O₂ ratio. At 20% O₂, the Co/Al interface is oxidized, leading to PMA and almost complete compensation of the demagnetizing field. Further increasing the O₂ ratio leads to a decrease of B_K^{eff} due to oxygen diffusing throughout the Co layer, as shown by the more pronounced decrease of B_K^{eff} after 14 days.

Overall, this set of data proves that the magnetic properties of Pt/Co/Al trilayers are extremely sensitive to the oxidation of both the top and bottom Co interfaces as well as to the oxygen concentration within the layers.

IV. SPIN-ORBIT TORQUES

In our experimental geometry, and to the lowest order in the unitary magnetization $\mathbf{m} = \mathbf{M}/M_s$, where

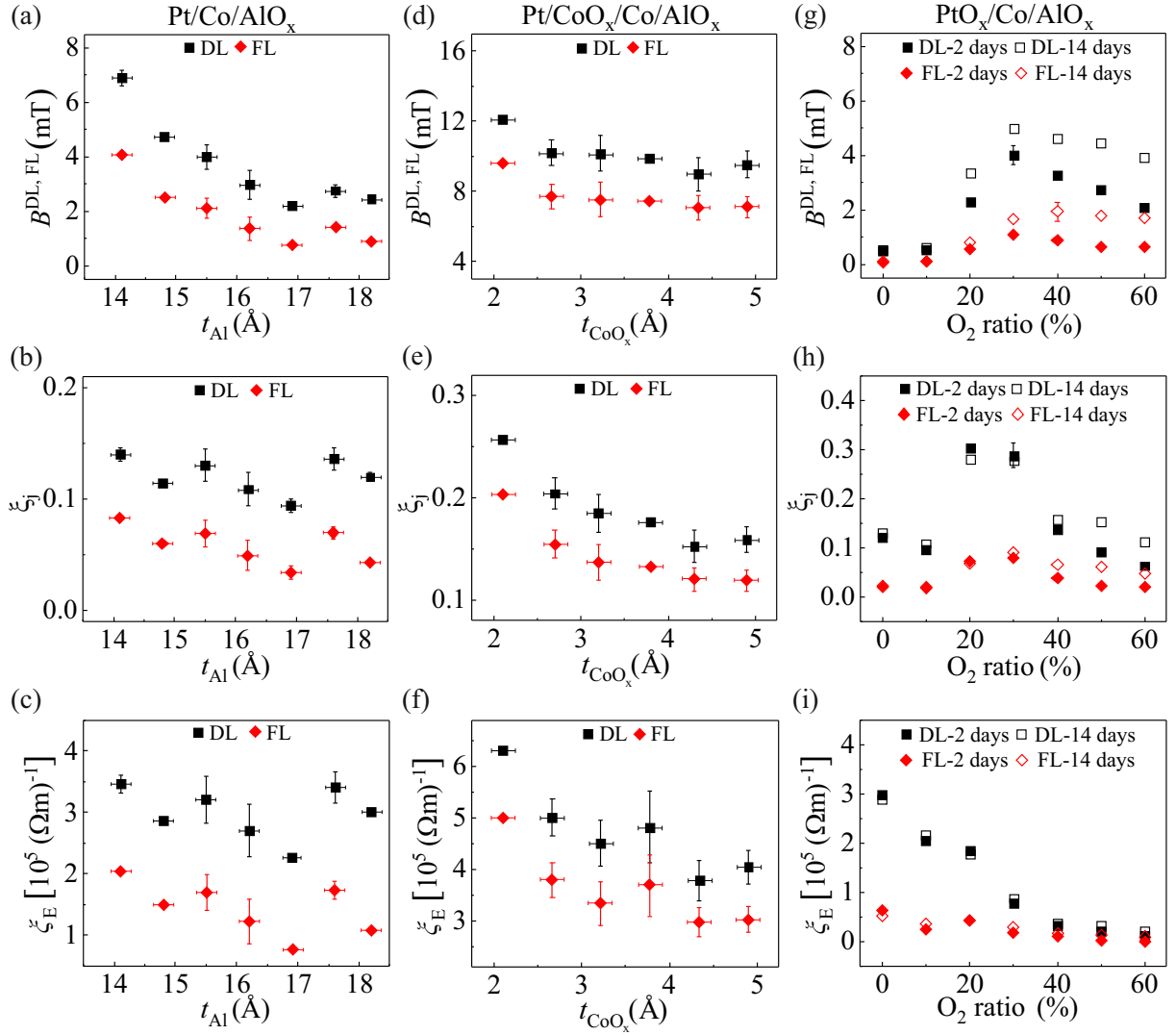


FIG. 6. (a) $B^{DL,FL}$, (b) $\xi_j^{DL,FL}$ and (c) $\xi_E^{DL,FL}$ as a function of t_{Al} in Pt/Co/AlO_x. (d-f) Same quantities as a function of t_{CoO_x} in Pt/CoO_x/Co/AlO_x and (g-i) O₂:(Ar+O₂) ratio in PtO_x/Co/AlO_x. The data shown as solid and open symbols in (g-i) were obtained, respectively, 2 and 14 days after the deposition of PtO_x/Co/AlO_x. Vertical error bars represent the standard deviation of the average of different devices from the same series. Horizontal error bars represent the uncertainty of the thickness calibration.

\mathbf{M} is the magnetization, the SOT is given by the sum of damping-like (DL) and field-like (FL) components [14, 17],

$$\mathbf{T} = T^{DL} \mathbf{m} \times (\mathbf{m} \times \mathbf{y}) + T^{FL} \mathbf{m} \times \mathbf{y}, \quad (2)$$

where \mathbf{y} represents the direction of the current-induced spin polarization. For characterization purposes, it is convenient to work with the two effective magnetic fields corresponding to the damping-like and field-like torques,

$$\mathbf{B}^{DL} = \mathbf{T}^{DL} \times \mathbf{m} = B^{DL}(\mathbf{m} \times \mathbf{y}), \quad (3)$$

$$\mathbf{B}^{FL} = \mathbf{T}^{FL} \times \mathbf{m} = B^{FL} \mathbf{y}. \quad (4)$$

The advantage of the effective field formulation is that their action on the magnetization can be directly compared to that of an external field of known magnitude

and direction, which allows for quantifying B^{DL} and B^{FL} by means of a variety of techniques [17]. Here we measure B^{DL} and B^{FL} using the harmonic Hall voltage method [14, 15, 41, 48]. A description of the method, representative second harmonic Hall resistance measurements of the different samples as well as the analysis of thermal voltages and planar Hall effect are reported in the Appendix. For simplicity, we focus on the effects of oxidation on the lowest order SOT terms (Eq. 2); a discussion of the higher order terms, i.e., of the angular dependence of the SOT, is given in Refs. 14, 29, 49, and 50.

The fields B^{DL} and B^{FL} scale inversely with the thickness of the ferromagnet. Therefore, in order to compare the SOT in different systems, we consider the SOT effi-

ciencies

$$\xi_j^{DL,FL} = \frac{2e}{\hbar} M_s t_{Co} \frac{B^{DL,FL}}{j}, \quad (5)$$

where t_{Co} is the thickness of the Co layer, \hbar the reduced Planck constant, and j the injected current density obtained by dividing the current by the cross section of the conductive layers. The current density applied to study the SOT in the Pt/Co/AlO_x and Pt/CoO_x/Co/AlO_x series was 1.0×10^7 A/cm², which was calculated by dividing the total current by the width of the Hall bar and the sum of the thickness of the Pt and Co layers, respectively, 6 and 5.65 nm. For the PtO_x/Co/AlO_x series, we applied a current of 1 mA, which corresponds to a current density of 1.7×10^6 A/cm² when considering both PtO_x(5) and Co(1) as the conductive layers.

Because the current distribution is not expected to be homogeneous in samples made of different layers with varying degrees of oxidation, we also consider the SOT efficiency per unit electric field [51]

$$\xi_E^{DL,FL} = \frac{2e}{\hbar} M_s t_{Co} \frac{B^{DL,FL}}{E} = \frac{\xi_j^{DL,FL}}{\rho}, \quad (6)$$

where $E = \rho j$ is the electric field and ρ is the resistivity. $\xi_E^{DL,FL}$ can be easily calculated by knowing the total magnetic moment measured by SQUID and is therefore independent of t_{Co} as well as on any assumption on the current distribution and the thickness of the conductive layers. When comparing samples with similar resistivity, it is equivalent to use either $\xi_j^{DL,FL}$ or $\xi_E^{DL,FL}$, which can be considered as an effective spin Hall angle and spin Hall conductivity, respectively. However, for samples with very different resistivities such as those belonging to the PtO_x/Co/AlO_x series, the electric field normalization provides a better means of comparison.

Figure 6 summarizes the results obtained on the three sample series for $B^{DL,FL}$, $\xi_j^{DL,FL}$, and $\xi_E^{DL,FL}$, which we discuss in detail below.

A. Pt/Co/AlO_x

Here we consider the effect of changing t_{Al} , hence the oxidation of the Co/Al interface, in the Pt/Co/AlO_x system. As shown in Fig. 6(a), the effective fields $B^{DL,FL}$ decrease monotonically as a function of t_{Al} . This decrease mostly reflects the increase of M_s as the Co layer changes from over- to under-oxidized (see Sec. III A). Accordingly, the SOT efficiencies show a weaker dependence on t_{Al} . $\xi_j^{DL,FL}$ and $\xi_E^{DL,FL}$ decrease slowly up to $t_{Al} = 16.9$ Å, and then increase rather abruptly from $t_{Al} = 16.9$ to 17.6 Å [Fig. 6(b,c)]. As the latter thickness corresponds to the optimal oxidation of the Co/AlO_x interface (see Sec. II B), we attribute the local maxima of $\xi_j^{DL,FL}$ and $\xi_E^{DL,FL}$ to the enhancement of the charge transfer and ensuing interfacial electric field between the Co and AlO_x layers. We note that this enhancement affects both the

damping-like and field-like components of the SOT, as expected from the spin current contributions originating from spin-orbit coupling and spin-dependent scattering at interfaces [52–54]. Moreover, the larger SOT efficiencies found for the optimized samples are consistent with the larger torques (torques per unit electric field and unit magnetization) calculated ab-initio for Pt/Co/O relative to Pt/Co/Al [55].

The sign of the field-like SOT is such that B^{FL} opposes the Oersted field generated by the current flowing the Pt layer. ξ_j^{DL} (ξ_j^{FL}) and ξ_E^{DL} (ξ_E^{FL}) peak at 0.14 (0.08) and 3.5 (2.1) $\times 10^5$ (Ωm)⁻¹, respectively, which compares well with the SOT efficiencies reported in previous studies of optimized Pt/Co/AlO_x [14]. Interestingly, these SOT efficiencies are consistently larger than those reported for Pt(5)/Co(1)/MgO(2), where ξ_j^{DL} (ξ_j^{FL}) = 0.11 (0.024) and ξ_E^{DL} (ξ_E^{FL}) = 2.43 (0.53) $\times 10^5$ (Ωm)⁻¹ [51]. Such a difference might be related to the different band alignment between Co and either AlO_x or MgO, leading to different interfacial electrical fields and scattering properties.

B. Pt/CoO_x/Co/AlO_x

Inserting a 2.1 Å thick CoO_x layer between Pt and Co leads to an enhancement of the SOT effective fields and efficiencies by about a factor 2 compared to the optimized Pt/Co/AlO_x trilayer [Fig. 6(d-f)]. This remarkable result indicates that the Pt/CoO_x and CoO_x/Co interfaces are very efficient in transferring spins from Pt to Co. Given that the Néel and blocking temperatures of CoO are well below room temperature in films thinner than 10 nm [56], the spin transfer across the insulating CoO_x layer is likely mediated by antiferromagnetic spin fluctuations, as found for the reciprocal effect of spin pumping in Y₃Fe₅O₁₂/NiO/Pt and Y₃Fe₅O₁₂/CoO/Pt trilayers [57, 58]. In such cases, a pronounced maximum of the pumping efficiency was reported when approaching the Néel temperature of the antiferromagnet [59]. Differently from these studies, however, here the FM layer is metallic and the spin current flows towards the FM, which is extremely promising for the efficient manipulation of the magnetization by an electric current. Additionally, we find that $\xi_j^{DL,FL}$ and $\xi_E^{DL,FL}$ decrease upon increasing the thickness of the CoO_x layer, consistently with diffusive spin transport mediated by correlated spin fluctuations [57]. Such a decrease shows that a significant fraction of the spin current giving rise to the SOT originates from either the Pt or the Pt/CoO_x interface. However, we also observe that $\xi_j^{DL,FL}$ and $\xi_E^{DL,FL}$ tend to saturate towards finite values rather than tending to zero, which may indicate that the CoO_x/Co interface also contributes to generating a spin current [52–54]. Overall, these results indicate that the insertion of a thin paramagnetic CoO_x layer significantly improves the charge-spin conversion efficiency of HM/FM/Ox structures at a very

small cost in terms of material engineering, consistently with recent reports [60, 61].

C. PtO_x/Co/AlO_x

The oxidation of Pt leads to a very different behavior compared to the oxidation of Co. Figures 6(g-i) show the SOT effective fields and efficiencies measured 2 days (full symbols) and 14 days (open symbols) after deposition of the PtO_x/Co/AlO_x series. Note that the values of $B^{DL,FL}$ at 0% O₂ ratio, i.e., for unoxidized Pt, are lower than reported for Pt/Co/AlO_x [Fig. 6(a)] because the current density employed in these measurements was about a factor 6 smaller compared to the Pt/Co/AlO_x series, whereas $\xi_j^{DL,FL}$ and $\xi_E^{DL,FL}$ are comparable. We recall also that changing the O₂ ratio from 0 to 30% O₂ leads to about a 10-fold increase of the resistance (Sec. II C) and R_{AHE} (Sec. III B) as well as to a 3-fold decrease of M_s (Sec. III A). The samples of these series have IMA, the strength of which varies with the O₂ ratio (Sec. III C).

Figure 6(g) shows that $B^{DL,FL}$ increase first by about a factor 10 as the O₂ ratio reaches 30% and then decrease by an amount that depends on the time elapsed between the deposition and the measurements. Samples measured 20 days after deposition show the same SOT compared with the measurements performed after 14 days, suggesting that the oxidation profiles becomes stable after several days. The initial increase of $B^{DL,FL}$ is partly assigned to the reduction of M_s , as shown by the comparatively smaller change of $\xi_j^{DL,FL}$ [Fig. 6(h)]. ξ_j^{DL} and ξ_j^{FL} peak at 0.30 and 0.07, respectively, close to 20% O₂ ratio. Our XPS measurements, however, show that Pt is not significantly oxidized at this ratio, as oxygen migrates towards the Co and Al layers (Sec. II B). A possible reason for this initial enhancement of $\xi_j^{DL,FL}$ could be the spontaneous formation of a CoO_x layer next to Pt, in analogy with the results reported in Sec. IV B. Yet, it is unlikely that oxygen migration will lead to the formation of a homogenous CoO_x layer between Pt and metallic Co, similar to the Pt/CoO_x/Co/AlO_x series. Further, measurements of the magnetic anisotropy suggest that oxygen reaches the Co/Al interface at around 20% O₂ ratio (Sec. III C). It is therefore likely that the peak of $\xi_j^{DL,FL}$ reflects a change of the current distribution in the PtO_x/Co/AlO_x layers rather than a true increase of the SOT efficiency. For example, if oxygen from the top-most part of the PtO_x layer migrates towards Al, most of the current will flow close to the Pt/Co interface, leading to an apparent increase of $\xi_j^{DL,FL}$. We recall that, for consistency between different samples, $\xi_j^{DL,FL}$ is calculated by assuming a constant cross-section for current flow, proportional to the total thickness of the PtO_x and Co layers.

Further insight into the dependence of the SOT on the O₂ ratio can be gained by analyzing the behavior of

$\xi_E^{DL,FL}$, which does not depend on the current distribution. Figure 6(i) shows that $\xi_E^{DL,FL}$ decreases monotonically with increasing O₂ ratio. Specifically, ξ_E^{DL} starts at $2.98 \times 10^5 (\Omega m)^{-1}$ at 0% O₂ and reaches $0.13 \times 10^5 (\Omega m)^{-1}$ at 60% O₂; ξ_E^{FL} shows a similar decreasing trend, from $0.63 \times 10^5 (\Omega m)^{-1}$ to $0.01 \times 10^5 (\Omega m)^{-1}$. According to Eq. 6, for measurements performed at constant current, $\xi_E^{DL,FL} \propto B^{DL,FL} M_s / R$. The strong decrease of $\xi_E^{DL,FL}$ is thus ascribed to the increment of R and reduction of M_s that occur upon augmenting the O₂ ratio.

Our results are in stark contrast with previous work carried out on PtO_x/Ni₈₁Fe₁₉/SiO₂ trilayers [34, 35], in which both $\xi_j^{DL,FL}$ and $\xi_E^{DL,FL}$ were found to increase monotonically with O₂ ratio, up to ξ_j^{DL} (ξ_j^{FL}) = 0.92 (0.19) and ξ_E^{DL} (ξ_E^{FL}) = $8.7 (1.8) \times 10^5 (\Omega m)^{-1}$ at 100% O₂. In the following, we discuss possible reasons for this discrepancy. First, the FM and cap layers are different, which may result in significant differences in both oxygen diffusion and oxidation profile as well as in the generation and transmission of spin currents at interfaces. Second, the measurements of $B^{DL,FL}$ in Refs. 34 and 35 were performed by spin-torque ferromagnetic resonance (FMR) and by measuring the broadening of the FMR lineshape upon dc current injection. The current and field normalizations required to calculate $\xi_j^{DL,FL}$ and $\xi_E^{DL,FL}$ in Refs. 34 and 35 were carried out by assuming current flow in the Ni₈₁Fe₁₉ layer only and constant resistance, respectively. The current normalization affects the absolute value of $\xi_j^{DL,FL}$, but would not induce a different trend as a function of O₂ ratio compared to ours, since we also assume a constant cross section for the current. The electric field normalization required to calculate $\xi_E^{DL,FL}$ is more critical, since the resistance increases continuously as a function of O₂ ratio in PtO_x/Ni₈₁Fe₁₉/SiO₂ [34]. However, even assuming a constant resistance, we do not observe a monotonous increase of $\xi_E^{DL,FL}$. We also note that assumptions on the distribution of the current as well as on the different contributions to the FMR lineshape can significantly affect the determination of the effective fields by spin-torque FMR [62]. Finally, no hints of post-deposition oxygen diffusion or changes of M_s were reported for either PtO_x/Ni₈₁Fe₁₉/SiO₂ or PtO_x/CoTb/MgO [34, 35], but also not specifically analyzed, which prevents a more stringent comparison with our results.

V. CURRENT-INDUCED SWITCHING

By increasing the current density beyond a critical threshold $j_c \approx 10^7 - 10^8$ A/cm², the SOT become large enough to reverse the magnetization of trilayers with strong PMA, such as Pt/Co/AlO_x [11, 63], Pt/Co/MgO [12], Ta/CoFeB/MgO [41, 64], and Pt/[Co/Ni]_N/Al [65]. Magnetization reversal is driven by the damping-like torque [11]; the field-like torque, which

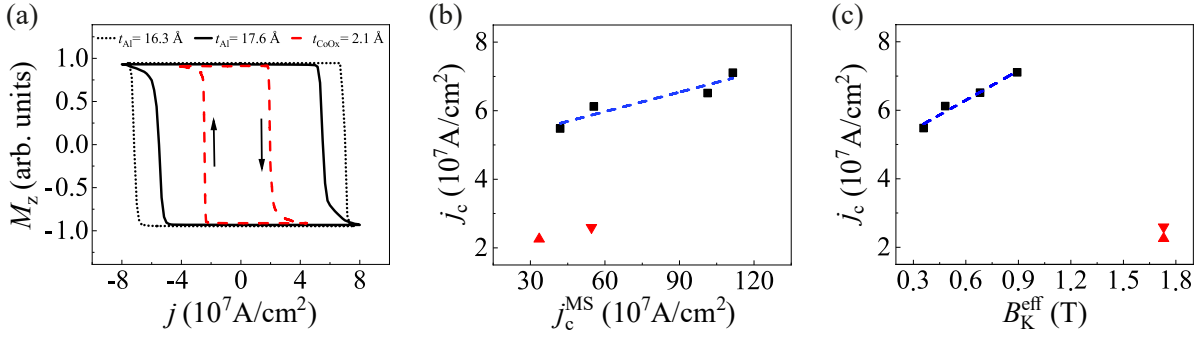


FIG. 7. (a) Out-of-plane component of the magnetization $M_z = R_H^\omega/R_{AHE}$ of Pt/Co/AlO $_x$ (dotted and solid black lines) and Pt/CoO $_x$ /Co/AlO $_x$ (red dashed line) as a function of dc current density during a switching loop. (b) j_c versus j_c^{MS} calculated using Eq. 7. (c) j_c as a function of B_K^{eff} . In (b) and (c) black squares and red triangles represent data for Pt/Co/AlO $_x$ and Pt/CoO $_x$ /Co/AlO $_x$, respectively. The dashed lines represent linear fits to j_c of Pt/Co/AlO $_x$. Up (down) triangles denote Pt/CoO $_x$ /Co/AlO $_x$ samples with $\xi_j^{DL} = 0.26$ (0.19). All data have been acquired in the presence of a constant field $B_x = +70$ mT for Pt/Co/AlO $_x$ and $B_x = +410$ mT for Pt/CoO $_x$ /Co/AlO $_x$. Note that j_c could not be measured for all the samples of the Pt/CoO $_x$ /Co/AlO $_x$ series as the specimens with thicker CoO $_x$ were irreversibly modified by the current.

is equivalent to a hard axis field, facilitates the switching by lowering the energy barrier for domain nucleation and propagation [7, 10, 66]. As the damping-like torque is perpendicular to both the current direction and the normal to the plane, an in-plane external field B_x parallel to the current is required in order to break the symmetry of the system and determine the polarity of the switching [11, 17]. In the macrospin approximation, the critical switching current is given by [67]

$$j_c^{MS} = \frac{2e}{\hbar} \frac{M_s t_{Co}}{\xi_j^{DL}} \left(\frac{B_K^{eff}}{2} - \frac{B_x}{\sqrt{2}} \right). \quad (7)$$

Although SOT-driven magnetization switching in structures with lateral dimensions larger than about 20 nm occurs by nucleation and expansion of magnetic domains [7, 24, 68–70], this expression provides a useful starting point to evaluate the dependence of j_c on critical material parameters.

In realistic systems, j_c depends on the parameters appearing in Eq. (7) as well as on the Dzyaloshinski-Moriya interaction, domain pinning field, device geometry, size, temperature, and duration of the current pulses [7, 63, 71–76]. The temperature, which is determined by the current distribution as well as by the thermal conductivity of the different materials in the stack, plays a major role, both in activating the switching as well as in changing critical parameters such as M_s , B_K , and ξ_j^{DL} during switching. These factors vary significantly, even among nominally similar material systems reported in the literature [17], so that a comparative study of the critical switching current versus magnetic anisotropy or SOT efficiency is hard to achieve. Here we use the controlled oxidation of the top Co interfaces in Pt/Co/AlO $_x$ in order to investigate such effects.

Figure 7(a) shows the switching of the out-of-plane magnetization of Pt/Co/AlO $_x$ with $t_{Al} = 16.3$ and 17.6 Å (dotted and solid black line, respectively) mea-

sured by the change of the anomalous Hall resistance during a sweep of a dc current in the presence of a constant field $B_x = +70$ mT. The curve represents the normalized signal $M_z = R_H^\omega/R_{AHE}$, where R_H^ω is the first harmonic Hall resistance (see Appendix). The dashed red line shows the switching of Pt/CoO $_x$ /Co/AlO $_x$ with $t_{CoO_x} = 2.1$ Å in the presence of a constant field $B_x = +410$ mT. The square loops indicate full switching of the magnetic layer with current in both types of samples. However, there are noticeable differences in the threshold current at which the magnetization switches, which we discuss below. In the following, the critical switching current density is defined as the current for which $M_z = 0$.

Figure 7(b) shows the experimental j_c versus the macrospin j_c^{MS} calculated using Eq. 7 for Pt/Co/AlO $_x$ (black squares) and Pt/CoO $_x$ /Co/AlO $_x$ (red triangles). As seen in Sec. III, reducing the oxidation of the top Co interface of Pt/Co/AlO $_x$ increases M_s and decreases B_K^{eff} by about a factor 4, whereas ξ_j^{DL} changes by about 40% depending on t_{Al} . Accordingly, we find that j_c scales linearly with j_c^{MS} , which in turn is proportional to M_s/ξ_j^{DL} times B_K^{eff} reduced by the constant in-plane field B_x . The plot further shows that j_c is about one order of magnitude smaller than predicted by j_c^{MS} and has a nonzero intercept for $j_c^{MS} \rightarrow 0$. The strong reduction of j_c compared to the macrospin threshold can be explained by the fact that magnetization reversal occurs by domain nucleation and propagation [7, 74] and is a thermally activated process [77], whereas Eq. 7 assumes coherent reversal at zero temperature. Further, the nonzero intercept of j_c denotes the presence of a finite activation barrier for switching. Accordingly, we find that the factor that mostly affects j_c is the strength of the magnetic anisotropy, as seen by the linear scaling of j_c with B_K^{eff} in Fig. 7(c).

Samples of the Pt/CoO $_x$ /Co/AlO $_x$ series have larger ξ_j^{DL} and B_K^{eff} relative to Pt/Co/AlO $_x$ and comparable

or smaller M_s . In Eq. 7 these factors partially compensate, such that j_c^{MS} of the Pt/CoO_x/Co/AlO_x samples with larger ξ_j^{DL} [red triangles in Fig. 7(b)] are close to the lower values of j_c^{MS} of the Pt/Co/AlO_x series [black squares in Fig. 7(b)]. However, the experimental j_c in Pt/CoO_x/Co/AlO_x is 30 to 40% that of Pt/Co/AlO_x. The different j_c in the two sample series can be possibly ascribed to the larger B_x employed to switch the high anisotropy Pt/CoO_x/Co/AlO_x samples. In models of spin-transfer torque switching, however, the barrier for magnetization reversal scales proportionally to $B_K^{\text{eff}}(1 - B_x/B_K^{\text{eff}})^2$ [78, 79]. This scaling does not account for the observed reduction of j_c in Pt/CoO_x/Co/AlO_x. Therefore, we conclude that either B_x has a stronger influence on SOT switching relative to spin transfer torque or there are other factors that promote switching in Pt/CoO_x/Co/AlO_x, such as the field-like torque and the Dzyaloshinskii-Moriya interaction, whose interplay cannot be discerned in our measurements.

VI. CONCLUSIONS

In summary, we investigated the oxidation effects on the resistivity, magnetization, magnetic anisotropy, anomalous Hall resistance, and SOT of Pt/Co/AlO_x, Pt/CoO_x/Co/AlO_x, and PtO_x/Co/AlO_x heterostructures. In all samples, increasing levels of oxidation lead to a reduction of M_s due to the formation of CoO_x. On the contrary, R_{AHE} decreases with increasing oxidation in Pt/Co/AlO_x but increases in Pt/CoO_x/Co/AlO_x and PtO_x/Co/AlO_x, consistently with the AHE being influenced by the magnetic volume as well as by spin-dependent scattering at oxidized interfaces.

The magnetic anisotropy is determined by the competition between the PMA of the Pt/Co and Co/Al interfaces and shape anisotropy. The latter scales as M_s and is strongly influenced by the oxidation of Co. In Pt/Co/AlO_x, B_K^{eff} decreases linearly with increasing t_{Al} , from 1.76 T to 0.36 T going from over-oxidized to under-oxidized Co/Al interfaces. Interestingly, the insertion of a thin CoO_x layer between Pt and Co results in very strong PMA of the Pt/CoO_x/Co/AlO_x series, with $B_K^{\text{eff}} \approx 1.7$ T, which is nearly independent on t_{CoO} . Direct oxidation of Pt, on the other hand, leads to a reduction of the PMA in PtO_x/Co/AlO_x compared to Pt/Co/AlO_x.

The amplitude of the damping-like and field-like SOT varies substantially depending on the oxidation profile, reflecting changes of M_s and SOT efficiency. For Pt/Co/AlO_x, we find that ξ_j^{DL} and ξ_j^{FL} peak at 0.14 and 0.07, respectively, upon optimal oxidation of the Co/Al interface, which corresponds to a maximum of M_s and minimum oxidation of Co, as confirmed by XPS. The insertion of a 2 Å thick paramagnetic CoO_x layer between Pt and Co nearly doubles ξ_j^{DL} and

ξ_j^{FL} , indicating that the overall spin conversion efficiency of Pt/CoO_x/Co/AlO_x is significantly higher than Pt/Co/AlO_x. Both ξ_j^{DL} and ξ_j^{FL} decrease with increasing t_{CoO_x} , but appear to level off around 0.15 and 0.12, respectively, for $t_{\text{CoO}_x} > 4$ Å. This trend suggests that not only the CoO_x layer enhances the transmission of the spin current generated by the Pt layer and Pt/CoO_x interface [57, 58, 60, 61], but also that the CoO_x/Co interface generates an additional spin accumulation that is independent of t_{CoO_x} .

The oxidation of the Pt layer leads to significant oxygen diffusion upon deposition of Co and Al, as confirmed by XPS and rationalized by the larger enthalpy of formation of Al₂O₃ and CoO relative to PtO. The inhomogeneous oxidation profile of the PtO_x/Co/AlO_x series prevents a clear cut determination of ξ_j^{DL} and ξ_j^{FL} , which remain, in any case, significantly smaller than reported for PtO_x/Ni₈₁Fe₁₉/SiO₂ [34, 35]. Additionally, the SOT efficiencies normalized by the electric field are found to decrease continuously with O₂ ratio. These results are in stark contrast with the SOT efficiency reported in Refs. 34 and 35, which shows a monotonic increase with increasing concentration of O₂. Possible explanations for such a discrepancy are discussed in Sec. IV C.

Finally, we proved that the critical current density required to switch the magnetization of the Co layer scales linearly with the theoretical current density calculated using the macrospin approximation, but is smaller by about one order of magnitude. This difference is attributed to an activated magnetization reversal process limited by the energy barrier for domain nucleation. The critical current density of Pt/Co/AlO_x is found to depend linearly on B_K^{eff} , which is determined by the degree of oxidation of the Co/Al interface. Owing to the large PMA, switching of Pt/CoO_x/Co/AlO_x generally requires the presence of a higher in-plane static field relative to Pt/Co/AlO_x. However, even when accounting for the different in-plane field, the critical current density of Pt/CoO_x/Co/AlO_x is lower than expected.

Our results demonstrate the critical impact of interfacial oxidation on the SOT and magnetotransport properties of HM/FM/Ox trilayers. Taken together with recent studies [23–28, 30–32, 60, 61], our work shows that devices with strongly improved PMA and charge-to-spin conversion efficiency might be realized by careful control of the oxidation of the top and bottom interfaces of the FM layer.

ACKNOWLEDGMENTS

We acknowledge funding from the the Swiss National Science Foundation (grant No. 200020-172775). We acknowledge Prof. N. Spencer for access to the surface analytical facilities. J. Feng was supported by a scholarship from the Chinese Scholarship Council.

Appendix A: Harmonic Hall voltage measurements

The anomalous Hall resistance, magnetic anisotropy, and SOT effective fields were measured using the harmonic Hall voltage method [14, 15, 17, 41, 48]. The method is based on the injection of an ac current $I = I_0 \cos(\omega t)$ with amplitude I_0 and frequency $f = \omega/2\pi$, typically about 10 Hz. As the magnetization oscillates around its equilibrium state due to the oscillating SOTs, the Hall resistance varies as $R_H(t) = R_H(\mathbf{B}_0 + \mathbf{B}_I)$, where \mathbf{B}_0 is the sum of the external field \mathbf{B}_{ext} and effective anisotropy field $\mathbf{B}_K^{\text{eff}}$, and \mathbf{B}_I is the sum of the current-induced effective fields \mathbf{B}^{DL} , \mathbf{B}^{FL} , and the Oersted field \mathbf{B}^{Oe} . In this situation, the Hall voltage can be written as

$$\begin{aligned} V_H &= I_0 \cos(\omega t) R_H(\mathbf{B}_0 + \mathbf{B}_I) \\ &= I_0 [R_H^0 + R_H^\omega \cos(\omega t) + R_H^{2\omega} \cos(2\omega t)]. \end{aligned} \quad (\text{A1})$$

Here, R_H^0 , R_H^ω , and $R_H^{2\omega}$ are the zeroth, first, and second harmonic Hall resistance, respectively. R_H^ω corresponds to the Hall resistance measured in a dc experiment, which is determined by the anomalous Hall effect (AHE) and planar Hall effect (PHE):

$$R_H^\omega = R_{\text{AHE}} \cos \theta + R_{\text{PHE}} \sin^2 \theta \sin(2\varphi), \quad (\text{A3})$$

where R_{AHE} and R_{PHE} are the AHE and PHE coefficients, respectively, and θ and φ are the polar and azimuthal angles of the magnetization, as defined in Fig. 1(e) of the main text. The ordinary Hall resistance is negligibly small in our samples compared with R_{AHE} and R_{PHE} , and ignored in the following. For samples with perpendicular magnetic anisotropy (PMA), namely Pt/Co/AlO_x and Pt/CoO_x/Co/AlO_x, R_{AHE} is given by half of the difference of the R_H^ω when the magnetization is up/down at $B_{\text{ext}} = 0$ [Fig. 8(a,b)]. For samples with in-plane magnetic anisotropy, namely PtO_x/Co/AlO_x, we swept B_{ext} out-of-plane up to 2.2 T magnetic field and estimated R_{AHE} as the intercept of the linear fit of the R_H^ω with the y -axis [Fig. 8(c)]. Examples of R_H^ω and $R_H^{2\omega}$ as a function of applied field for samples of the three series with different oxidation levels are shown in Fig. 8.

1. Measurement of B_K^{eff}

The effective magnetic anisotropy field (Eq. 1) is determined from the field dependence of R_H^ω reported in Fig. 8(a-c). For the samples with PMA, B_K^{eff} is given by

$$B_K^{\text{eff}} = \left| \frac{\cos \theta_B}{\cos \theta} - \frac{\sin \theta_B}{\sin \theta} \right| B_{\text{ext}}, \quad (\text{A4})$$

where θ_B is the polar angle of the applied field, which is set prior to the measurement, and θ is obtained from Eq. A3. This equation assumes that the magnetization behaves as a macrospin in a uniaxial anisotropy field,

which is approximately correct as long as R_H^ω has a reversible behavior versus the external field.

All the samples of the PtO_x/Co/AlO_x series have in-plane magnetic anisotropy ($B_K^{\text{eff}} < 0$), which cannot be estimated using the method described above. An approximate estimate of B_K^{eff} in this series can be obtained by measuring the field required to saturate the magnetization along the out-of-plane hard-axis. In the macrospin approximation, such a field corresponds to the sum of the demagnetizing field and magnetocrystalline anisotropy field, as given in Eq. 1. The hard axis saturation field is obtained by the crossing point of the two lines that fit R_H^ω at high field and in the low field region where the magnetization coherently rotates from in-plane to out-of-plane [Fig. 8(c)].

2. Measurement of B^{DL} and B^{FL}

a. Samples with perpendicular magnetic anisotropy

For samples with PMA, the dependence of $R_H^{2\omega}$ on the current is conveniently expressed as [14, 41]

$$\begin{aligned} R_H^{2\omega} &= [R_{\text{AHE}} - 2R_{\text{PHE}} \cos \theta \sin(2\varphi)] \frac{d \cos \theta}{d\mathbf{B}_I} \cdot \mathbf{B}_I \\ &\quad + R_{\text{PHE}} \sin^2 \theta \frac{d \sin(2\varphi)}{d\mathbf{B}_I} \cdot \mathbf{B}_I + R_{\nabla T} \sin \theta \cos \varphi, \end{aligned} \quad (\text{A5})$$

where $\mathbf{B}_I = \mathbf{B}^{DL} + \mathbf{B}^{FL} + \mathbf{B}^{\text{Oe}}$ and $R_{\nabla T}$ is the thermal resistance due to the out-of-plane temperature gradient $\nabla T \propto I_0^2$ induced by Joule heating [41]. In principle, both the anomalous Nernst effect (ANE) and the spin Seebeck effect can contribute to $R_{\nabla T}$. However, in metal bilayers, the ANE is expected to dominate. In the latter case, one has $R_{\nabla T} = \alpha \nabla T / I_0$, where α is the anomalous Nernst constant in units of VmK^{-1} . The angle dependent thermal resistance must be subtracted from $R_H^{2\omega}$ in order to avoid overestimating the SOTs, as described later.

In order to measure the first order contributions to the SOT, it is sufficient to consider the limit of small oscillations of the magnetization about the out-of-plane direction ($\theta \approx 0^\circ$). In such a case, B^{DL} and B^{FL} are obtained as follows [15, 48]

$$B_{\theta \approx 0^\circ}^{DL, FL} = -2 \frac{\partial (R_H^{2\omega} - R_{\nabla T} \sin \theta \cos \varphi)}{\partial B_{\varphi=0^\circ, 90^\circ}} / \frac{\partial^2 R_H^\omega}{\partial B_{\varphi=0^\circ, 90^\circ}^2} \quad (\text{A6})$$

where $\frac{\partial (R_H^{2\omega} - R_{\nabla T} \sin \theta \cos \varphi)}{\partial B_{\varphi=0^\circ, 90^\circ}}$ is the derivative of $R_H^{2\omega} - R_{\nabla T} \sin \theta \cos \varphi$ as a function of external field and $\frac{\partial^2 R_H^\omega}{\partial B_{\varphi=0^\circ, 90^\circ}^2}$ is the second derivative of R_H^ω as a function of external field ($\theta \approx 0^\circ$, and $\varphi = 0^\circ$ for B^{DL} , $\varphi = 90^\circ$ for B^{FL}). The thermal component $R_{\nabla T} \sin \theta \cos \varphi$ in the numerator of Eq. A6 must be subtracted from $R_H^{2\omega}$ prior to evaluating the fields, as detailed in Sec. A 2 c.

If $R_{\text{PHE}} \ll R_{\text{AHE}}$, Eq. A6 is sufficient to quantify the SOTs effective fields, which are proportional to the ratio

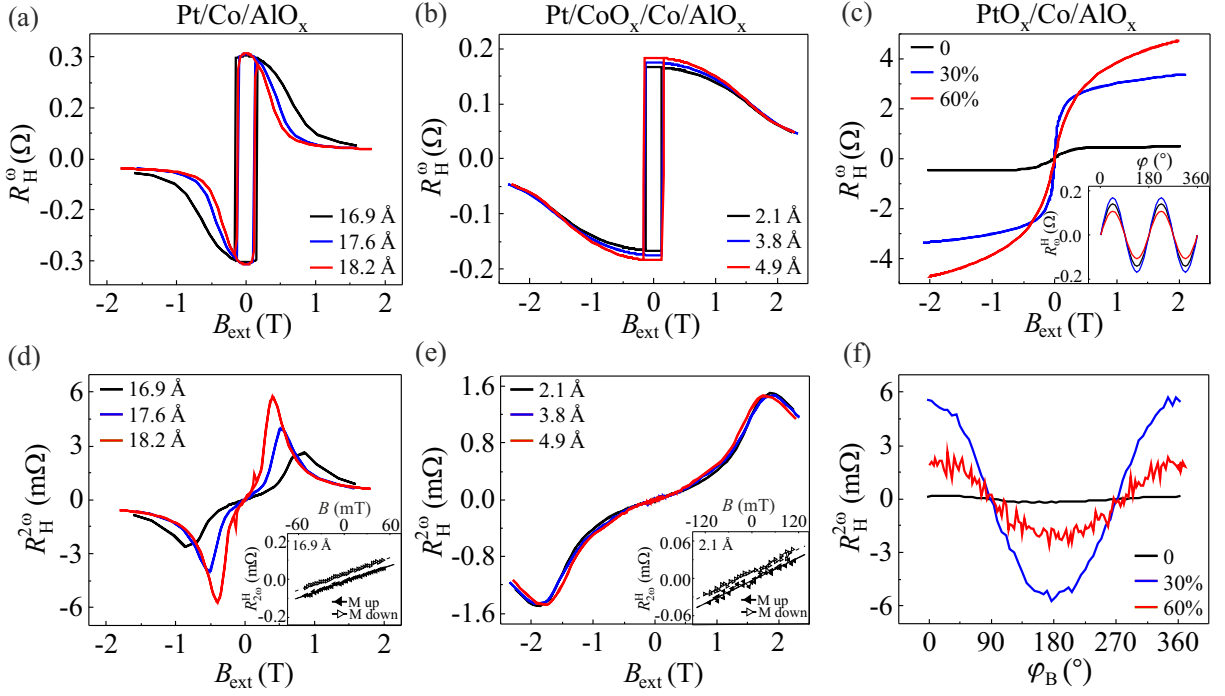


FIG. 8. R_H^ω as a function of external field for (a) Pt/Co/AlO_x with different t_{Al} , (b) Pt/CoO_x/Co/AlO_x with different t_{CoO_x} , and (c) PtO_x/Co/AlO_x with different O₂:(Ar+O₂) ratios. (d,e) $R_H^{2\omega}$ measured simultaneously with the curves shown in (a,b). Close ups of the low field behavior of R_H^ω for the two systems are shown in the insets. (f) $R_H^{2\omega}$ as a function of φ_B for PtO_x/Co/AlO_x, measured simultaneously with the angle scans of R_H^ω shown in the inset of (c). For Pt/Co/AlO_x and Pt/CoO_x/AlO_x, the external field is applied at angles $\theta_B = 86^\circ$ and $\varphi_B = 0^\circ$. For PtO_x/Co/AlO_x, the field is applied at $\theta_B = 0^\circ$. The in-plane angle scans in (f) are performed by rotating the samples in a constant field of 1 T.

of the current-dependent Hall susceptibility and a normalization factor that accounts for the tendency of the magnetization to remain aligned along the easy axis. If R_{PHE} cannot be ignored, a correction to Eq. A6 is required [14, 48], which gives

$$B^{DL,FL} = \frac{B_{\theta \approx 0^\circ}^{DL,FL} \pm 2rB_{\theta \approx 0^\circ}^{FL,DL}}{1 - 4r^2}, \quad (\text{A7})$$

where $r = R_{\text{PHE}}/R_{\text{AHE}}$. Figure 9 shows that R_{PHE} is relatively large in all the samples investigated in this work, with the larger values found in the PtO_x/Co/AlO_x series. The overall trend of R_{PHE} is similar to that of R_{AHE} discussed in Sect. III of the main text, despite the different origin of the PHE and AHE. The similar behavior is attributed to the fact that both effects depend on the volume fraction and M_s of metallic Co as well as on the current distribution in the multilayer structure. In most samples, r attains values between 0.3 and 0.4, such that Eq. A7 is used to determine the fields B^{DL} and B^{FL} .

b. Samples with in-plane magnetic anisotropy

In order to quantify the SOTs in samples with in-plane magnetic anisotropy we performed harmonic Hall voltage measurements by rotating the sample in the xy plane

and applying a sufficiently large external field (with various amplitudes) to ensure the magnetic saturation of the sample is along the field direction. In this geometry, assuming that the in-plane magnetization is isotropic, $R_H^{2\omega}$ is given by [41]:

$$R_H^{2\omega} = (R_{\text{AHE}} \frac{B^{DL}}{B_{\text{ext}} - B_{\text{K}}^{\text{eff}}} + R_{\nabla T}) \cos \varphi + 2R_{\text{PHE}}(2 \cos^3 \varphi - \cos \varphi) \frac{B^{FL} + B^{\text{Oe}}}{B_{\text{ext}}}. \quad (\text{A8})$$

By symmetry, there are two contributions to the above signal, the first one is proportional to $\cos \varphi$ and depends on both the DL-SOT and thermal voltage, and the second one is proportional to $2R_{\text{PHE}}(2 \cos^3 \varphi - \cos \varphi)$ and depends on the FL-SOT. The fields B^{DL} and B^{FL} are found using the fitting procedure described below.

c. Determination of $R_{\nabla T}$

We fit Eq. A8 as a function of φ by the sum of two functions proportional to $\cos \varphi$ and $(2 \cos^3 \varphi - \cos \varphi)$ and obtain two coefficients, $(R_{\text{AHE}} \frac{B^{DL}}{B_{\text{ext}} - B_{\text{K}}^{\text{eff}}} + R_{\nabla T})$ and $\frac{B^{FL} + B^{\text{Oe}}}{B_{\text{ext}}}$. This procedure is repeated for each value of B_{ext} . Plotting these two coefficients as a function of

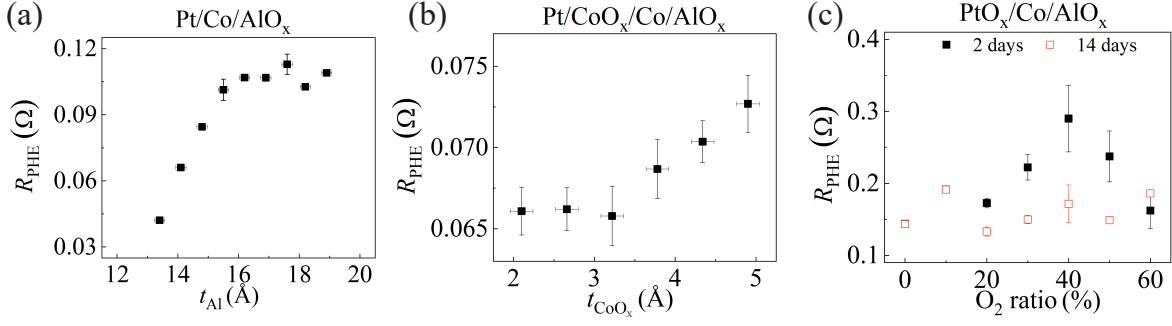


FIG. 9. R_{PHE} in (a) Pt/Co/AlO_x, (b) Pt/CoO_x/Co/AlO_x, and (c) PtO_x/Co/AlO_x. The data shown as solid and open symbols in (c) were obtained, respectively, 2 and 14 days after the deposition of PtO_x/Co/AlO_x.

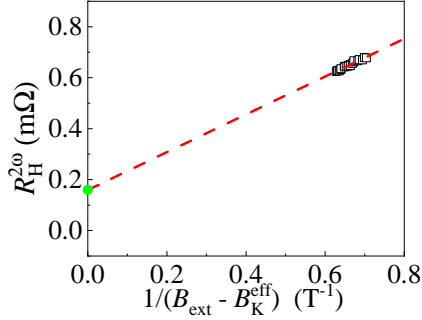


FIG. 10. Separation of B^{DL} and thermal signal from $R_H^{2\omega}$ for Pt(5)/Co(1)/AlO_x. Plot of the cosine component of $R_H^{2\omega}$ as a function of $\frac{1}{B_{\text{ext}} - B_K^{\text{eff}}}$ measured in a field scan performed at $\varphi = 45^\circ$ with current density 1.0×10^7 A/cm². The intercept (green dot) of the linear fit is the thermal resistance $R_{\nabla T}$.

$\frac{1}{B_{\text{ext}} - B_K^{\text{eff}}}$ and $\frac{1}{B_{\text{ext}}}$ yields a linear curve with slopes corresponding to B^{DL} and B^{FL} , respectively. Finally, the intercept of $(R_{\text{AHE}} \frac{B^{DL}}{B_{\text{ext}} - B_K^{\text{eff}}} + R_{\nabla T})$ vs. $\frac{1}{B_{\text{ext}} - B_K^{\text{eff}}}$ gives the thermal resistance $R_{\nabla T}$ [41]. We note that here B^{FL} is the sum of SOT and Oersted field contributions. The latter is calculated as $B^{\text{Oe}} = \mu_0 j_{\text{Pt}} t_{\text{Pt}} / 2$, where j_{Pt} is the current density flowing in Pt and t_{Pt} is the Pt thickness [14, 80]. For a current density of 1.0×10^7 A/cm² in Pt(5)/Co(1)/AlO_x we thus find $B^{\text{Oe}} = 0.31$ mT. Note that Fig. 6 in the main text includes B^{Oe} as well.

Equation A8 and the analysis described above are equally valid for samples with PMA as long as the magnetization is fully saturated in-plane by applying an external field B_{ext} larger than B_K^{eff} . Alternative to the angle scan measurements, which are time consuming, an easier way to determine the thermal resistance and B^{DL} in samples with PMA is by performing an in-plane field sweep along $\varphi = 45^\circ$ at magnetic saturation (i.e., $B_{\text{ext}} > B_K^{\text{eff}}$). In this measurement, the second term on the right hand side of Eq. A8 vanishes by symmetry since $2 \cos^3 \varphi - \cos \varphi = 0$. After subtracting a magnetically irrelevant offset, the data are plotted as a function of $\frac{1}{B_{\text{ext}} - B_K^{\text{eff}}}$, which allows one to obtain B^{DL} and $R_{\nabla T}$ at $\varphi = 45^\circ$, as shown

in Fig. 10.

Figure 11 reports the values of $R_{\nabla T}$ in the three sample series. We observe that $R_{\nabla T}$ is approximately constant in Pt/Co/AlO_x, independently of t_{Al} . This behavior differs from that of the AHE [see Fig. 4(d) in the main text], which is the electrical counterpart of the ANE. A possible reason for this discrepancy is the different direction of the electric field driving the AHE, which is in-plane, and the thermal gradient driving the ANE, which is out-of-plane. Moreover, since the current distribution is not significantly altered by the oxidation of the top interface, we expect that the thermal gradient remains approximately constant in this series. In Pt/CoO_x/Co/AlO_x, we find that $R_{\nabla T}$ varies by less than 20% as a function of t_{CoO_x} , similar to the AHE [see Fig. 4(e) in the main text]. This small variation likely reflects the fact that neither the current distribution nor the interfaces vary significantly in this system. On the other hand, $R_{\nabla T}$ changes strongly as a function of the O₂:(Ar+O₂) ratio in PtO_x/Co/AlO_x, closely reflecting the trend observed for the AHE [see Fig. 4(f) in the main text]. We believe that oxygen migration in this system disrupts the layered structure of the conducting elements, resulting in a more isotropic electrical and thermal conductivity compared to Pt/Co/AlO_x. Interestingly, the sign of $R_{\nabla T}$ is inverted in PtO_x/Co/AlO_x relative to Pt/Co/AlO_x and Pt/CoO_x/Co/AlO_x. We have no clear explanation for this effect, other than surmising the inversion of the thermal gradient in PtO_x/Co/AlO_x, which might be due to a change of the current distribution in the Pt and Co layers relative to Pt/Co/AlO_x and Pt/CoO_x/Co/AlO_x.

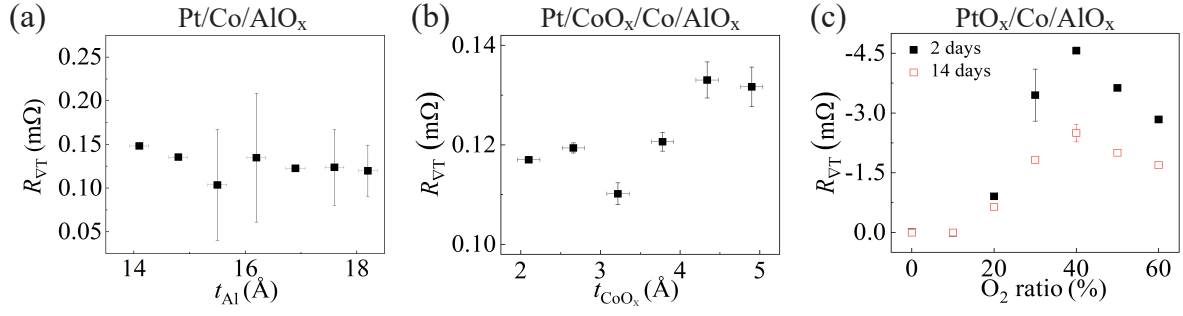


FIG. 11. $R_{\nabla T}$ in (a) Pt/Co/AlO_x, (b) Pt/CoO_x/Co/AlO_x, and (c) PtO_x/Co/AlO_x. The measurements have been performed by using the in-plane field sweep method at $\varphi = 45^\circ$ for the samples with PMA (a,b) and the angle scan method for the samples with in-plane magnetic anisotropy (c). The data shown as solid and open symbols in (c) were obtained, respectively, 2 and 14 days after the deposition of PtO_x/Co/AlO_x.

- [1] S. Ikeda, K. Miura, H. Yamamoto, K. Mizunuma, H. D. Gan, M. Endo, S. Kanai, J. Hayakawa, F. Matsukura, and H. Ohno, A perpendicular-anisotropy CoFeB – MgO magnetic tunnel junction, *Nat. Mater.* **9**, 721 (2010).
- [2] A. Brataas, A. D. Kent, and H. Ohno, Current-induced torques in magnetic materials, *Nat. Mater.* **11**, 372 (2012).
- [3] M. Cubukcu, O. Boulle, M. Drouard, K. Garello, C. O. Avci, I. M. Miron, J. Langer, B. Ocker, P. Gambardella, and G. Gaudin, Spin-orbit torque magnetization switching of a three-terminal perpendicular magnetic tunnel junction, *Appl. Phys. Lett.* **104**, 042406 (2014).
- [4] D. Apalkov, B. Dieny, and J. M. Slaughter, Magnetoresistive random access memory, *Proceedings of the IEEE* **104**, 1796 (2016).
- [5] S. Monso, B. Rodmacq, S. Auffret, G. Casali, F. Fetta, B. Gilles, B. Dieny, and P. Boyer, Crossover from in-plane to perpendicular anisotropy in Pt/CoFe/AlOx sandwiches as a function of Al oxidation: A very accurate control of the oxidation of tunnel barriers, *Appl. Phys. Lett.* **80**, 4157 (2002).
- [6] J. P. Pellegren and V. M. Sokalski, Thickness and interface-dependent crystallization of CoFeB alloy thin films, *IEEE Transactions on Magnetics* **51**, 1 (2015).
- [7] M. Baumgartner, K. Garello, J. Mendil, C. O. Avci, E. Grimaldi, C. Murer, J. Feng, M. Gabureac, C. Stamm, Y. Acremann, S. Finizio, S. Wintz, J. Raabe, and P. Gambardella, Spatially and time-resolved magnetization dynamics driven by spin-orbit torques, *Nat. Nanotech.* **12**, 980 (2017).
- [8] G. Jan, L. Thomas, S. Le, Y. Lee, H. Liu, J. Zhu, R. Tong, K. Pi, Y. Wang, D. Shen, R. He, J. Haq, J. Teng, V. Lam, K. Huang, T. Zhong, T. Torng, and P. Wang, Demonstration of fully functional 8mb perpendicular stt-mram chips with sub-5ns writing for non-volatile embedded memories, in *2014 Symposium on VLSI Technology (VLSI-Technology): Digest of Technical Papers* (2014) pp. 1–2.
- [9] K. Garello, F. Yasin, S. Couet, L. Souriau, J. Swerts, S. Rao, S. Van Beek, W. Kim, E. Liu, S. Kundu, D. Tsvetanova, K. Croes, N. Jossart, E. Grimaldi, M. Baumgartner, D. Crotti, A. Fummont, P. Gambardella, and G. S. Kar, Sot-mram 300mm integration for low power and ultrafast embedded memories, in *2018 IEEE Symposium on VLSI Circuits* (2018) pp. 81–82.
- [10] I. M. Miron, G. Gaudin, S. Auffret, B. Rodmacq, A. Schuhl, S. Pizzini, J. Vogel, and P. Gambardella, Current-driven spin torque induced by the Rashba effect in a ferromagnetic metal layer, *Nat. Mater.* **9**, 230 (2010).
- [11] I. M. Miron, K. Garello, G. Gaudin, P. J. Zermatten, M. V. Costache, S. Auffret, S. Bandiera, B. Rodmacq, A. Schuhl, and P. Gambardella, Perpendicular switching of a single ferromagnetic layer induced by in-plane current injection, *Nature* **476**, 189 (2011).
- [12] C. O. Avci, K. Garello, I. M. Miron, G. Gaudin, S. Auffret, O. Boulle, and P. Gambardella, Magnetization switching of an MgO/Co/Pt layer by in-plane current injection, *Appl. Phys. Lett.* **100**, 212404 (2012).
- [13] L. Liu, C.-F. Pai, Y. Li, H. W. Tseng, D. C. Ralph, and R. A. Buhrman, Spin-torque switching with the giant spin hall effect of tantalum, *Science* **336**, 555 (2012).
- [14] K. Garello, I. M. Miron, C. O. Avci, F. Freimuth, Y. Mokrousov, S. Blugel, S. Auffret, O. Boulle, G. Gaudin, and P. Gambardella, Symmetry and magnitude of spin-orbit torques in ferromagnetic heterostructures, *Nat. Nanotech.* **8**, 587 (2013).
- [15] J. Kim, J. Sinha, M. Hayashi, M. Yamanouchi, S. Fukami, T. Suzuki, S. Mitani, and H. Ohno, Layer thickness dependence of the current-induced effective field vector in Ta|CoFeB|MgO, *Nat. Mater.* **12**, 240 (2013).
- [16] M. Cubukcu, O. Boulle, N. Mikuszeit, C. Hamelin, T. Brcher, N. Lamard, M. Cyrille, L. Buda-Prejbeanu, K. Garello, I. M. Miron, O. Klein, G. de Loubens, V. V. Naletov, J. Langer, B. Ocker, P. Gambardella, and G. Gaudin, Ultra-fast perpendicular spinorbit torque mram, *IEEE Transactions on Magnetics* **54**, 1 (2018).
- [17] A. Manchon, J. Železný, I. M. Miron, T. Jungwirth, J. Sinova, A. Thiaville, K. Garello, and P. Gambardella, Current-induced spin-orbit torques in ferromagnetic and antiferromagnetic systems, *Rev. Mod. Phys.* **91**, 035004 (2019).
- [18] S. Zhang, P. M. Levy, and A. Fert, Mechanisms of spin-polarized current-driven magnetization switching, *Phys. Rev. Lett.* **88**, 236601 (2002).
- [19] A. Manchon, C. Ducruet, L. Lombard, S. Auffret, B. Rodmacq, B. Dieny, S. Pizzini, J. Vogel, V. Uhl, M. Hochstrasser, and G. Panaccione, Analysis of oxygen induced anisotropy crossover in trilayers Pt/Co/MO_x, *J. Appl. Phys.* **104**, 043914 (2008).
- [20] B. Rodmacq, A. Manchon, C. Ducruet, S. Auffret, and B. Dieny, Influence of thermal annealing on the perpendicular magnetic anisotropy of Pt/Co/AlOx trilayers, *Phys. Rev. B* **79**, 024423 (2009).
- [21] D. Chiba, S. Fukami, K. Shimamura, N. Ishiwata, K. Kobayashi, and T. Ono, Electrical control of the ferromagnetic phase transition in cobalt at room temperature, *Nat. Mater.* **10**, 853 (2011).
- [22] H. Garad, L. Ortega, A. Y. Ramos, Y. Joly, F. Fetta, S. Auffret, B. Rodmacq, B. Diny, O. Proux, and A. I. Erko, Competition between CoOx and CoPt phases in Pt/Co/AlOx semi tunnel junctions, *J. Appl. Phys.* **114**, 053508 (2013).
- [23] G. Yu, P. Upadhyaya, Y. Fan, J. G. Alzate, W. Jiang, K. L. Wong, S. Takei, S. A. Bender, L. T. Chang, Y. Jiang, M. Lang, J. Tang, Y. Wang, Y. Tserkovnyak, P. K. Amiri, and K. L. Wang, Switching of perpendicular magnetization by spin-orbit torques in the absence of external magnetic fields, *Nat. Nanotech.* **9**, 548 (2014).
- [24] G. Yu, L.-T. Chang, M. Akyol, P. Upadhyaya, C. He, X. Li, K. L. Wong, P. K. Amiri, and K. L. Wang, Current-driven perpendicular magnetization switching in Ta/CoFeB/[TaO_x or MgO/TaO_x] films with lateral structural asymmetry, *Appl. Phys. Lett.* **105**, 102411 (2014).
- [25] X. Qiu, K. Narayanapillai, Y. Wu, P. Deorani, D.-H. Yang, W.-S. Noh, J.-H. Park, K.-J. Lee, H.-W. Lee, and H. Yang, Spin-orbit-torque engineering via oxygen manipulation, *Nat. Nanotech.* **10**, 333 (2015).
- [26] C.-F. Pai, Y. Ou, L. H. Vilela-Leão, D. C. Ralph, and R. A. Buhrman, Dependence of the efficiency of spin hall

- torque on the transparency of Pt/ferromagnetic layer interfaces, *Phys. Rev. B* **92**, 064426 (2015).
- [27] M. Akyol, J. G. Alzate, G. Yu, P. Upadhyaya, K. L. Wong, A. Ekicibil, P. Khalili Amiri, and K. L. Wang, Effect of the oxide layer on current-induced spin-orbit torques in Hf|CoFeB|MgO and Hf|CoFeB|TaOx structures, *Appl. Phys. Lett.* **106**, 032406 (2015).
- [28] Y. Hibino, T. Hirai, K. Hasegawa, T. Koyama, and D. Chiba, Enhancement of the spin-orbit torque in a Pt/Co system with a naturally oxidized Co layer, *Appl. Phys. Lett.* **111**, 132404 (2017).
- [29] H. K. Gweon, K.-J. Lee, and S. H. Lim, Influence of MgO sputtering power and post annealing on strength and angular dependence of spin-orbit torques in Pt/Co/MgO trilayers, *Phys. Rev. Applied* **11**, 014034 (2019).
- [30] U. Bauer, L. Yao, A. J. Tan, P. Agrawal, S. Emori, H. L. Tuller, S. van Dijken, and G. S. D. Beach, Magnetoionic control of interfacial magnetism, *Nat. Mater.* **14**, 174 (2014).
- [31] S. Emori, U. Bauer, S. Woo, and G. S. D. Beach, Large voltage-induced modification of spin-orbit torques in Pt/Co/GdOx, *Appl. Phys. Lett.* **105**, 222401 (2014).
- [32] C. Bi, Y. Liu, T. Newhouse-Illige, M. Xu, M. Rosales, J. W. Freeland, O. Mryasov, S. Zhang, S. G. E. te Velthuis, and W. G. Wang, Reversible control of Co magnetism by voltage-induced oxidation, *Phys. Rev. Lett.* **113**, 267202 (2014).
- [33] K.-U. Demasius, T. Phung, W. Zhang, B. P. Hughes, S.-H. Yang, A. Kellock, W. Han, A. Pushp, and S. S. P. Parkin, Enhanced spin-orbit torques by oxygen incorporation in tungsten films, *Nat. Commun.* **7**, 10644 (2016).
- [34] H. An, Y. Kanno, A. Asami, and K. Ando, Giant spin-torque generation by heavily oxidized Pt, *Phys. Rev. B* **98**, 014401 (2018).
- [35] H. An, T. Ohno, Y. Kanno, Y. Kageyama, Y. Monnai, H. Maki, J. Shi, and K. Ando, Current-induced magnetization switching using an electrically insulating spin-torque generator, *Sci. Adv.* **4**, eaar2250 (2018).
- [36] A. Dua, V. George, and R. Agarwala, Characterization and microhardness measurement of electron-beam-evaporated alumina coatings, *Thin Solid Films* **165**, 163 (1988).
- [37] Y. Nagano, Standard enthalpy of formation of platinum hydrous oxide, *J. Therm. Anal. Calorim.* **69**, 831 (2002).
- [38] D. D. Wagman, J. D. Cox, and V. A. Medvedev, *CO-DATA key values for thermodynamics* (Hemisphere Pub. Corp., 1989).
- [39] R. D. Holmes, H. S. O'Neill, and R. J. Arculus, Standard gibbs free energy of formation for Cu₂O, NiO, CoO, and Fe_xO: High resolution electrochemical measurements using zirconia solid electrolytes from 9001400 K, *Geochim. Cosmochim. Acta* **50**, 2439 (1986).
- [40] C. O. Avci, G. S. D. Beach, and P. Gambardella, Effects of transition metal spacers on spin-orbit torques, spin hall magnetoresistance, and magnetic anisotropy of pt/co bilayers, *Phys. Rev. B* **100**, 235454 (2019).
- [41] C. O. Avci, K. Garello, M. Gabureac, A. Ghosh, A. Fuhrer, S. F. Alvarado, and P. Gambardella, Interplay of spin-orbit torque and thermoelectric effects in ferromagnet/normal-metal bilayers, *Phys. Rev. B* **90**, 224427 (2014).
- [42] See supplementary materials for more details on the determination of the Hall voltage, magnetic anisotropy, and SOT effective fields.
- [43] S. L. Zhang, J. Teng, J. Y. Zhang, Y. Liu, J. W. Li, G. H. Yu, and S. G. Wang, Large enhancement of the anomalous hall effect in Co/Pt multilayers sandwiched by MgO layers, *Appl. Phys. Lett.* **97**, 222504 (2010).
- [44] J. Y. Zhang, Z. L. Wu, S. G. Wang, C. J. Zhao, G. Yang, S. L. Zhang, Y. Liu, S. Liu, J. Teng, and G. H. Yu, Effect of interfacial structures on anomalous hall behavior in perpendicular Co/Pt multilayers, *Appl. Phys. Lett.* **102**, 102404 (2013).
- [45] H. X. Yang, M. Chshiev, B. Dieny, J. H. Lee, A. Manchon, and K. H. Shin, First-principles investigation of the very large perpendicular magnetic anisotropy at fe|mgo and co|mgo interfaces, *Phys. Rev. B* **84**, 054401 (2011).
- [46] W. S. Chung, S. M. Yang, T. W. Kim, and J. P. Hong, Ultrathin Co-O oxide layer-driven perpendicular magnetic anisotropy in a CoO/[Co/Pd]m multilayer matrix upon annealing, *Sci. Rep.* **6**, 37503 (2016).
- [47] C. Pan, H. An, T. Harumoto, Z. Zhang, Y. Nakamura, and J. Shi, Control of the perpendicular magnetic anisotropy and perpendicular exchange bias in CoPt/CoOx thin films, *J. Magn. Magn. Mater.* **484**, 320 (2019).
- [48] M. Hayashi, J. Kim, M. Yamanouchi, and H. Ohno, Quantitative characterization of the spin-orbit torque using harmonic hall voltage measurements, *Phys. Rev. B* **89**, 144425 (2014).
- [49] C. O. Avci, K. Garello, C. Nistor, S. Godey, B. Ballesteros, A. Mugarza, A. Barla, M. Valvidares, E. Pellegrin, A. Ghosh, I. M. Miron, O. Boulle, S. Auffret, G. Gaudin, and P. Gambardella, Fieldlike and antidamping spin-orbit torques in as-grown and annealed ta/cofeb/mgo layers, *Phys. Rev. B* **89**, 214419 (2014).
- [50] K. D. Belashchenko, A. A. Kovalev, and M. van Schilfgaarde, First-principles calculation of spin-orbit torque in a co/pt bilayer, *Phys. Rev. Materials* **3**, 011401 (2019).
- [51] M. H. Nguyen, D. C. Ralph, and R. A. Buhrman, Spin torque study of the spin hall conductivity and spin diffusion length in platinum thin films with varying resistivity, *Phys. Rev. Lett.* **116**, 126601 (2016).
- [52] V. P. Amin and M. D. Stiles, Spin transport at interfaces with spin-orbit coupling: Phenomenology, *Phys. Rev. B* **94**, 104420 (2016).
- [53] V. P. Amin and M. D. Stiles, Spin transport at interfaces with spin-orbit coupling: Formalism, *Phys. Rev. B* **94**, 104419 (2016).
- [54] V. P. Amin, J. Zemen, and M. D. Stiles, Interface-generated spin currents, *Phys. Rev. Lett.* **121**, 136805 (2018).
- [55] F. Freimuth, S. Blügel, and Y. Mokrousov, Spin-orbit torques in Co/Pt(111) and Mn/W(001) magnetic bilayers from first principles, *Phys. Rev. B* **90**, 174423 (2014).
- [56] T. Ambrose and C. L. Chien, Dependence of exchange coupling on antiferromagnetic layer thickness in NiFe/CoO bilayers, *J. Appl. Phys.* **83**, 6822 (1998).
- [57] C. Hahn, G. de Loubens, V. V. Naletov, J. B. Youssef, O. Klein, and M. Viret, Conduction of spin currents through insulating antiferromagnetic oxides, *Europhys. Lett.* **108**, 57005 (2014).
- [58] Z. Qiu, J. Li, D. Hou, E. Arenholz, A. T. NDiaye, A. Tan, K.-i. Uchida, K. Sato, S. Okamoto, Y. Tserkovnyak, Z. Q. Qiu, and E. Saitoh, Spin-current probe for phase transition in an insulator, *Nat. Commun.* **7**, 12670 (2016).
- [59] W. Lin, K. Chen, S. Zhang, and C. L. Chien, Enhancement of thermally injected spin current through an an-

- tiferromagnetic insulator, *Phys. Rev. Lett.* **116**, 186601 (2016).
- [60] K. Hasegawa, Y. Hibino, M. Suzuki, T. Koyama, and D. Chiba, Enhancement of spin-orbit torque by inserting CoO_x layer into Co/Pt interface, *Phys. Rev. B* **98**, 020405 (2018).
- [61] H. Wang, J. Finley, P. Zhang, J. Han, J. T. Hou, and L. Liu, Spin-orbit-torque switching mediated by an antiferromagnetic insulator, *Phys. Rev. Applied* **11**, 044070 (2019).
- [62] M. Harder, Y. Gui, and C.-M. Hu, Electrical detection of magnetization dynamics via spin rectification effects, *Phys. Rep.* **661**, 1 (2016).
- [63] K. Garello, C. O. Avci, I. M. Miron, M. Baumgartner, A. Ghosh, S. Auffret, O. Boulle, G. Gaudin, and P. Gambardella, Ultrafast magnetization switching by spin-orbit torques, *Appl. Phys. Lett.* **105**, 212402 (2014).
- [64] C. Zhang, M. Yamanouchi, H. Sato, S. Fukami, S. Ikeda, F. Matsukura, and H. Ohno, Magnetization reversal induced by in-plane current in Ta/CoFeB/MgO structures with perpendicular magnetic easy axis, *J. Appl. Phys.* **115**, 17C714 (2014).
- [65] J.-C. Rojas-Sánchez, P. Laczkowski, J. Sampaio, S. Collin, K. Bouzehouane, N. Reyren, H. Jaffrs, A. Mougin, and J.-M. George, Perpendicular magnetization reversal in Pt/[Co/Ni]₃/Al multilayers via the spin hall effect of Pt, *Appl. Phys. Lett.* **108**, 082406 (2016).
- [66] T. Taniguchi, S. Mitani, and M. Hayashi, Critical current destabilizing perpendicular magnetization by the spin hall effect, *Phys. Rev. B* **92**, 024428 (2015).
- [67] K.-S. Lee, S.-W. Lee, B.-C. Min, and K.-J. Lee, Threshold current for switching of a perpendicular magnetic layer induced by spin Hall effect, *Appl. Phys. Lett.* **102**, 112410 (2013).
- [68] S. Emori, U. Bauer, S.-M. Ahn, E. Martinez, and G. S. D. Beach, Current-driven dynamics of chiral ferromagnetic domain walls, *Nat. Mater.* **12**, 611 (2013).
- [69] K.-S. Ryu, L. Thomas, S.-H. Yang, and S. Parkin, Chiral spin torque at magnetic domain walls, *Nat. Nanotech.* **8**, 527 (2013).
- [70] C. K. Safeer, E. Ju, A. Lopez, L. Buda-Prejbeanu, S. Auffret, S. Pizzini, O. Boulle, I. M. Miron, and G. Gaudin, Spin-orbit torque magnetization switching controlled by geometry, *Nat. Nanotech.* **11**, 143 (2015).
- [71] O. J. Lee, L. Q. Liu, C. F. Pai, Y. Li, H. W. Tseng, P. G. Gowtham, J. P. Park, D. C. Ralph, and R. A. Buhrman, Central role of domain wall depinning for perpendicular magnetization switching driven by spin torque from the spin hall effect, *Phys. Rev. B* **89**, 024418 (2014).
- [72] C. Zhang, S. Fukami, S. DuttaGupta, H. Sato, and H. Ohno, Time and spatial evolution of spin-orbit torque-induced magnetization switching in W/CoFeB/MgO structures with various sizes, *Jpn. J. Appl. Phys.* **57**, 04FN02 (2018).
- [73] T. H. Pham, S.-G. Je, P. Vallobra, T. Fache, D. Lacour, G. Malinowski, M. C. Cyrille, G. Gaudin, O. Boulle, M. Hehn, J.-C. Rojas-Sánchez, and S. Mangin, Thermal contribution to the spin-orbit torque in metallic-ferrimagnetic systems, *Phys. Rev. Applied* **9**, 064032 (2018).
- [74] N. Mikuszeit, O. Boulle, I. M. Miron, K. Garello, P. Gambardella, G. Gaudin, and L. D. Buda-Prejbeanu, Spin-orbit torque driven chiral magnetization reversal in ultrathin nanostructures, *Phys. Rev. B* **92**, 144424 (2015).
- [75] M. A. Laguna-Marco, P. Kayser, J. A. Alonso, M. J. Martínez-Lope, M. van Veenendaal, Y. Choi, and D. Haskel, Electronic structure, local magnetism, and spin-orbit effects of Ir(IV)-, Ir(V)-, and Ir(VI)- based compounds, *Phys. Rev. B* **91**, 214433 (2015).
- [76] S. Pizzini, J. Vogel, S. Rohart, L. D. Buda-Prejbeanu, E. Jué, O. Boulle, I. M. Miron, C. K. Safeer, S. Auffret, G. Gaudin, and A. Thiaville, Chirality-induced asymmetric magnetic nucleation in Pt/Co/ AlO_x ultrathin microstructures, *Phys. Rev. Lett.* **113**, 047203 (2014).
- [77] E. Grimaldi, V. Krizakova, G. Sala, F. Yasin, S. Couet, G. Kar, K. Garello, and P. Gambardella, Single-shot dynamics of spinorbit torque and spin transfer torque switching in three-terminal magnetic tunnel junctions, *Nat. Nanotechnol.* (2020).
- [78] R. H. Koch, J. A. Katine, and J. Z. Sun, Time-resolved reversal of spin-transfer switching in a nanomagnet, *Phys. Rev. Lett.* **92**, 088302 (2004).
- [79] T. Seki, S. Mitani, and K. Takahashi, Nucleation-type magnetization reversal by spin-polarized current in perpendicularly magnetized fept layers, *Phys. Rev. B* **77**, 214414 (2008).
- [80] A. Ghosh, K. Garello, C. O. Avci, M. Gabureac, P. Gambardella, Interface-Enhanced Spin-Orbit Torques and Current-Induced Magnetization Switching of Pd/Co/ AlO_x Layers , *Phys. Rev. Appl.* **7**, 014004 (2017).